1-1-2010

Development of a Portable Cavity Ring-Down Spectroscopic Technique for Measuring Stable Isotopes in Atmospheric Methane

Gregory A. Bostrom
Portland State University

Recommended Citation

Bostrom, Gregory A., "Development of a Portable Cavity Ring-Down Spectroscopic Technique for Measuring Stable Isotopes in Atmospheric Methane" (2010). *Dissertations and Theses.* Paper 51.
https://doi.org/10.15760/etd.51

Development of a Portable Cavity Ring-Down Spectroscopic Technique for Measuring

Stable Isotopes in Atmospheric Methane

by

Gregory A. Bostrom

A thesis submitted in partial fulfillment of the
requirements for the degree of

Master of Science
in
Physics

Thesis Committee:
Andrew Rice
Dean Atkinson
Aslam Khalil
Erik Sanchez
Todd Rosenstiel

Portland State University
©2010

Abstract

Trace gases can have a significant impact on the Earth's climate, and the analysis of changes in these gases and an understanding of how much of these changes are a result of human activity is important for understanding global climate change. Methane (CH_4) is the second only to CO_2 in radiative forcing over the last 200 years, and its concentration in the atmosphere has more than doubled since 1750. Sources and sinks of CH_4 have characteristic isotopic effects, which shift the relative concentration of the methane isotopologues. Spectroscopic techniques for of analysis the isotopic composition of methane have been evolving since the early 1990's, and promise real-time, in-situ measurements that would provide unprecedented information on the methane atmospheric cycle. Here we present our development and results of a new optical spectroscopic isotope ratio instrument using cavity ringdown spectroscopy in the near IR region using the $\nu_2+2\nu_3$ overtone band. This region has limited interference from other molecules, and an advantageous juxtaposition of a $^{13}CH_4$ triplet, and a single $^{12}CH_4$ peak, allowing near-simultaneous measurement of both isotopologues. We present the results of two datasets showing high linearity over a wide range of isotope ratios, which achieved a precision of ±4‰. We present analysis of the data and consider the effects of temperature and molecular interference.

Table of Contents

List of Tables

List of Figures

I. Introduction/Background

The analysis of trace gases in the atmosphere provides valuable information on mankind's effect on Earth's climate. Methane (CH_4) is the most important anthropogenically influenced greenhouse gas after carbon dioxide (CO_2) (Ramanathan, 1985), and has more than doubled in concentration since the industrial revolution (Rasmussen, 1984). Ice-core measurements of CH_4 concentrations indicate that levels have varied between 0.4 ppm and 0.8 ppm over the 650,000 years leading up to the industrial revolution. In contrast, CH_4 concentrations have been increased from 0.700 ppm in 1750, to a level of 1.774 ppm in 2007 (IPCC, 2007, Ch. 2). This substantial change has been attributed to anthropogenic contributions: estimates of CH_4 sources in 1750 attribute 10% of the CH_4 emissions to anthropogenic sources, while present day estimates suggest total CH_4 emissions have nearly doubled since 1750, and anthropogenic sources now account for 60% of the emissions (IPCC, 2007, Ch. 7).

In recent decades the rate of increase in CH_4 concentration has exhibited a decrease from about 1%/yr (or 14 ppb/yr) in 1985 to almost 0%/yr in 2005. The growth rate during this period shows high interannual variability, with a maximum of 14 ppb/yr in 1998 and a minimum of -4 ppb/yr in 2004 (IPCC, 2007, Ch. 2). These recent changes in CH_4 growth rate remain incompletely understood and are the subject of debate (see e.g., Simpson, 2002; Dlugokencky, 2003; Bousquet, 2006). This adds significant uncertainty to projections of future CH_4 concentrations, and the applicability of some IPCC's scenarios which predict CH_4 concentrations will increase to levels between 2 and 3.5 ppmv by the end of the century (IPCC, 2007)).

CH$_4$ has a significant greenhouse effect, with a strong absorption band at 7.66 μm in the mid-IR region. It is in this region (~10 μm) where the Earth's radiative heat emission peaks, preventing energy from radiating into space, and the atmospheric CH$_4$ re-emits more than half of the energy towards the surface. Increasing concentrations result in increased absorption of this energy, which then raises the temperature of the earth. If we assume a steady state condition in the energy balance prior to the industrial revolution, then the radiative forcing (W/m^2) reflects the impact of this change on the energy balance due to changes in atmospheric constituents, and can be negative (cooling) or positive (warming). The best estimate of radiative forcing for CH$_4$ is 0.48 W/m^2, which is significant compared to estimates of 1.66 W/m^2 for CO$_2$ and a total for all low-level greenhouse gases (not including H$_2$O) of 2.6 W/m^2 (IPCC, 2007).

In addition to the direct effect of IR absorption, the oxidation of CH$_4$ can have significant impacts on both the troposphere and stratosphere. CH$_4$ reacts with OH, and therefore can lower the OH concentration. Since OH is the major oxidizer of many molecules in the atmosphere, such as non-methane hydrocarbons, sulfur containing compounds, and halocarbons, and many other pollutants and greenhouse gases, reduction in OH concentrations due to reaction with increased concentrations of CH$_4$ can increase the atmospheric lifetimes of these other molecules (Weubbles, et.al., 2000). This amplifies their effects in the atmosphere. In addition, oxidation of CH$_4$ produces CO$_2$, H$_2$O (this reaction is the major source of stratospheric H$_2$O), and CO (producing approximately 25% of tropospheric levels), and formaldehyde (CH$_2$O). It also indirectly impacts O$_3$ levels in areas with high concentrations of NO$_x$ molecules (Wuebbles, 2000).

The major emissions of CH_4 are from bacterial sources in a variety of environments: anoxic soils (wetlands, rice paddies), animal (including livestock and termites) ruminant, and waste. Thermogenic methane sources (fossil fuel activities including natural gas losses, oil drilling, and coal processing) and biomass burning are the next major sources of CH_4. In addition to these two major groups of sources, there are also minor contributions from oceans and methane clathrate hydrates (Tyler et.al., 2007; Whiticar, 2000; Reeburgh, 2003). Many of the important CH_4 sources and their respective contributions are shown in Table 1. The IPCC (2007) summarized the latest publications (2000-2007) estimating CH_4 sources and showed a range of 264-428 Tg/yr for anthropogenic sources and 145-260 Tg/yr for natural sources. These sources will be discussed in more detail in Section I.3. At steady-state the rate of production is balanced by the rate of consumption by the CH_4 sinks (approximately 70% is consumed by tropospheric reaction with OH), which will be discussed in the Section I.4. If CH_4 is not in a steady state condition, then there will be a net increase or decrease in the atmospheric CH_4 concentration. This increase leads to the increased absorption of outgoing IR radiation and results in radiative forcing.

Table 1 CH$_4$ sources, their annual emissions and isotopic signatures. Data taken from (Tyler et.al., 2007) and supplemented (grayed values in table) by (Whiticar, 2000).

Source	Emission (Tg/yr)	δ13C	δD
Tundra	10	-65	-320
Lakes (bogs, fens, lakes)	75	-59	-322
Swamps & Marshes	106	-56	-322
Rice Paddies	80	-59	-323
Animals	95	-62	-305
Landfills	42	-50	-293
Gas Venting and Leakage	54	-38	-175
Oceans (coastal margins)	10	-40	-220
Coal Mining	27	-37	-175
Biomass Burning	45	-26	-210
Termites	20	-57	-390
Gas Hydrates	10	-52	-240
Atmospheric Background (NH)	*?*	*-47.4*	*-96*
Atmospheric Background (SH)	*?*	*-47.2*	*-86*
Mean Source	?	**-52**	**-287**

I.2 Isotopic analysis

Isotopic analysis of atmospheric CH$_4$, determining the isotopic compositions of its elements to a high degree of accuracy and precision, provides insight into the processes that produce (sources) and processes that consume (sinks) CH$_4$, and their relative impacts on atmospheric concentrations. This is because each source and each sink imparts a characteristic isotopic "fingerprint" to emitted or consumed CH$_4$.

A detailed theoretical explanation of isotopic effects due to molecular reactions can be found in Wolfsberg (1972) and Bigeleisen and Wolfsberg (1958). Briefly, the mass difference between the isotopes causes a change in the relative reaction rate for different isotopologues. At temperatures on the order of 300K, the most significant effect the isotope substitution has on the reaction rate is due to the change in the vibrational

zero-point energy of the two reactant molecules. The larger mass will have a lower energy, since $E_{0,V} \propto \mu^{-\frac{1}{2}}$ (where μ is the reduced mass for the molecular bond) if we assume harmonic motion, and therefore will require more energy to reach the transition state. For CH_4, we expect a substitution of D for H (86% increase in μ) to have a more significant effect on the reaction rates than the substitution of ^{13}C for ^{12}C (0.6% increase in μ). Additional factors that affect the reaction rates are: changes in the bond strength (force constant) of the bond with isotopic substitution, higher level vibrational state contributions to the partition function, and quantum tunneling, which is especially important for hydrogen. This difference between the abundant and rare isotopes results in a change in the ratio of isotopes between the reactants and the products. The terms enrichment and depletion imply an increase and decrease in the amount of the rarer isotope, respectively.

Isotopic ratios (rare isotope/most abundant isotope) are expressed relative to an internationally recognized standard reference ratio—the deviation from the standard is given by the δ-notation, e.g., for $^{13}C/^{12}C$:

$$\delta^{13}C = \left(\left(\frac{\left[^{13}C \right]}{\left[^{12}C \right]} \right)_{sample} \bigg/ \left(\frac{\left[^{13}C \right]}{\left[^{12}C \right]} \right)_{standard} - 1 \right) \cdot 1000 \qquad (1)$$

$$\delta D = \left(\left(\frac{\left[D \right]}{\left[H \right]} \right)_{sample} \bigg/ \left(\frac{\left[D \right]}{\left[H \right]} \right)_{standard} - 1 \right) \cdot 1000 \qquad (2)$$

Where $\left(\dfrac{[^{13}C]}{[^{12}C]}\right)_{sample}$ and $\left(\dfrac{[^{13}C]}{[^{12}C]}\right)_{standard}$ are the ratio of the concentrations of ^{13}C to ^{12}C for

the sample and standard, respectively; and $\left(\dfrac{[D]}{[H]}\right)_{sample}$ and $\left(\dfrac{[D]}{[H]}\right)_{standard}$ are the ratio of

concentrations of D to H for the sample and standard, respectively. The factor of 1000

indicates that values are given in "per mil" (‰) and this notation has been adopted for

stating δ values, where the standard for $\delta^{13}C$ is the Vienna Peedee Belemnite (VPDB)

ratio of 0.0112372, and the standard for δD is the Vienna Surface Mean Ocean Water

(VSMOW) ratio of 0.00015574 (de Laeter, et.al., 2003). Current background $\delta^{13}C$-CH_4

values are -47.4‰ for the northern hemisphere and -47.2‰ for the southern hemisphere

(Stevens and Wahlen, 2000). Similarly, the δD-CH_4 for background atmosphere is -86‰

for the southern hemisphere and -96‰ for the northern hemisphere (Stevens and Wahlen,

2000).

I.3 Isotopic signatures of CH_4 Sources

From Table 1 we can see that bacterial production of CH_4 is responsible for

approximately 75% of the CH_4 emission. The process by which organic matter is

converted to methane by bacteria is qualitatively shown in Figure 1, and involves the

breakdown of organic matter along two different paths, and different bacteria perform

each of the three different steps. The production of CH_4 via CO_2 reduction accounts for

approximately 30% of the production in anoxic soils and sediments (acetate fermentation

accounts for the remaining 70%), and nearly 100% of the production from animals

(Boone, 2000). There are two major factors that determine the isotopic signature of biological sources: (1) enzymatic reactions tend to be faster for the lighter isotopes (higher reaction rate constant), and therefore produce CH_4 that is depleted (more negative $\delta^{13}C$) than its reactants, and (2) the $\delta^{13}C$ of the organic matter and other reactants (Boone, 2000) which are used to produce CH_4. Organic matter will be depleted with respect to the standard (geologic) carbon, with $\delta^{13}C$ ranging from -35‰ to -10‰. The methanogenesis process further reduces the $\delta^{13}C$, giving biogenic source $\delta^{13}C$ values in the range -70‰ to -45‰ (Boone, 2000; Tyler, 1991).

For bacterial sources the δD depends on the pathway that generates the CH_4. For CO_2 reduction, the H (or D) atoms come from H_2O, and therefore δD depends on the KIE for the reduction reaction and the δD of the reacted H_2O. For acetate fermentation, the methyl (CH_3) remains intact, and therefore only 25% may be directly related to the δD in the formation H_2O (Whiticar, 1999). However, one expects the organic matter itself to have a δD related to the reacted H_2O as well.
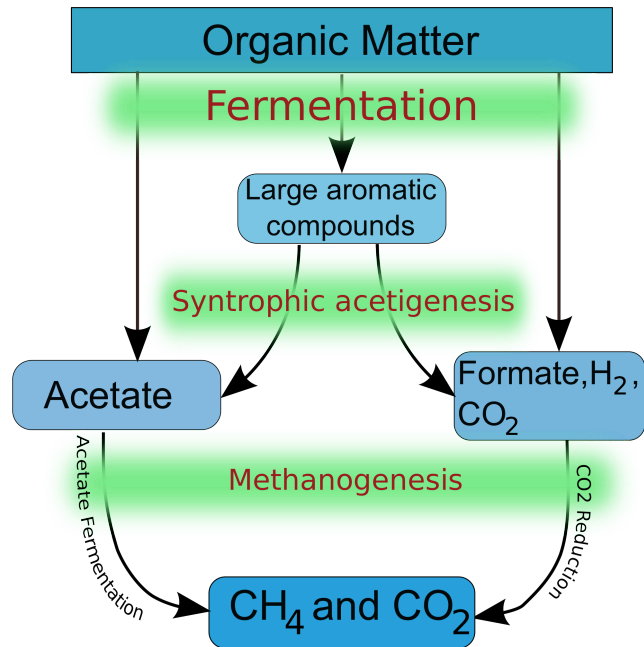
Figure 1 Diagram depicting the different microbial processes for converting organic matter to CH_4 (adapted from Boone, 2000).

Thermogenic methane sources (fossil fuel activities including natural gas losses, oil drilling, and coal processing) and biomass burning are the next major sources of CH_4. Similar to the discussion above, the isotopic signature of the fossil fuels and biomass burning will be depleted with respect to the geologic $\delta^{13}C$, since they are derived from organic matter, with values ranging from -45‰ to -20‰. The significant depletion evident in the δD (-250‰ to -100‰) of these thermogenic sources from their organic origins has been attributed for fossil CH_4 coming into hydrogen exchange equilibrium during the conversion from organic material to CH_4 (Schoell, 1980). In addition to these major groups of sources, there are also minor contributions from oceans ($\delta^{13}C$ = -40‰,

δD =-220‰) and methane clathrate hydrates ($\delta^{13}C$ = -52‰, δD =-240‰) (Tyler et.al., 2007; Whiticar, 2000; Reeburgh, 2003).

A useful way of visualizing the isotopic signatures is to plot both the $\delta^{13}C$ and δD simultaneously, as shown in Figure 2. This highlights the separation between the different sources, as well as a comparison to the current measured background levels. CH_4 emitted from the various sources have distinctive isotope ratios, which are significantly different from the background atmosphere. In fact, looking at the mass weighted average of the source isotopic signatures (shown in Figure 2), it is apparent that the ambient isotope ratio (also shown in Figure 2) cannot be achieved solely through direct mixing of the sources. The isotope effects of the CH_4 sinks play a significant role in moving from source to background levels (Whiticar, 2000).
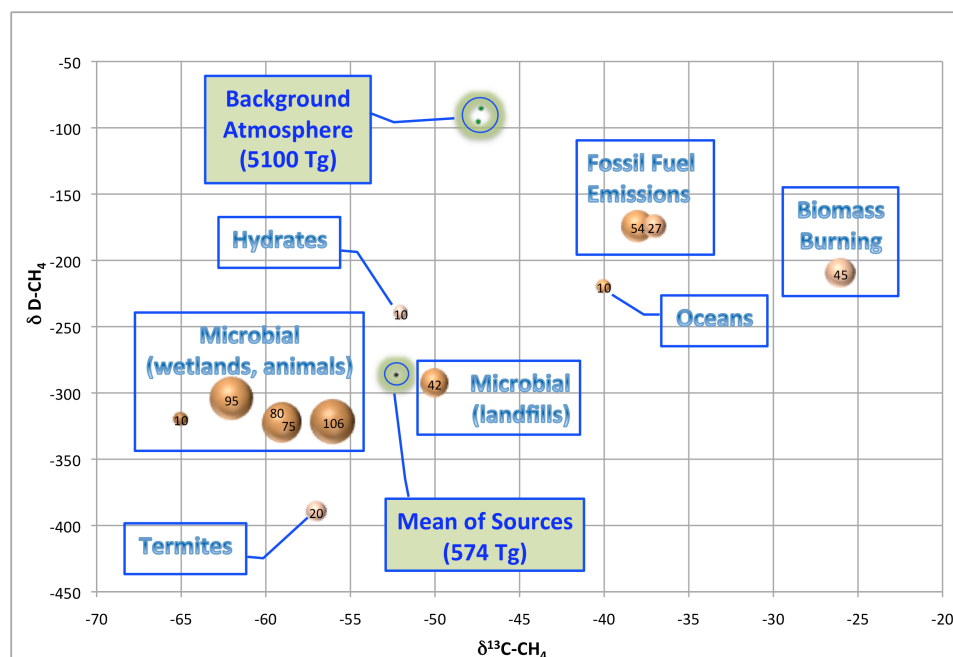
Figure 2 Isotopic signatures of methane sources listed in **Table 1**. The anthropogenic sources (fossil fuel, biomass burning, and landfills) are discernible from the natural sources and the ambient background. The size of the circle indicates the emission strength (Tg/yr) of individual sources. Data taken from (Tyler et.al., 2007) and supplemented (grayed values in table) by (Whiticar, 2000). For reference, the weighted average of the sources and the background atmosphere are also shown.

I.4 CH$_4$ sinks and their isotopic effects

According to their assessment in 2007, the IPCC reports that there is currently only a +1 Tg/yr difference (imbalance) between CH$_4$ source and sinks, and the major CH$_4$ sink (more than 70%) is the reaction with OH in the troposphere (see reaction R1). The remaining sinks of atmospheric CH$_4$ are (a) methanotrophic bacteria which aerobically oxidize CH$_4$ in oxic soils (in forest areas and grasslands, for example), and (b) transport to the stratosphere and subsequent reactions with OH, Cl (reaction R2), and O(^1D) (reaction R3).

$$CH_4 + OH \rightarrow CH_3 + H_2O \qquad\qquad (R1)$$

$$Cl + CH_4 \rightarrow HCl + CH_3 \qquad\qquad (R2)$$

$$O(^1D) + CH_4 \rightarrow CH_3 + OH \qquad\qquad (R3)$$

The kinetic isotope effect (KIE), α, is defined as the ratio of the reaction rate coefficients for the abundant isotope to the rare isotope. These effects are dominated by mass-dependent isotope fractionation, in which the lighter isotope reacts faster (has a higher rate constant) than the heavier isotope, and therefore generally $\alpha > 1$, which leaves the remaining CH_4 less depleted (higher delta = more enriched). Thus, in general the enrichment process in the oxidation of CH_4 opposes the depletion of the production cycle, as one might expect. The actual fractionation factors for each process are difficult to determine accurately, and small uncertainties have a significant impact on the interpretation of source and sink effects. More detailed laboratory studies of the KIEs are necessary to more fully characterize the effect of the sinks on atmospheric $\delta^{13}C$ and δD. For the three oxidation reactions given above, the best estimates for the sink effects on CH_4 are shown in Table 2. The amount of CH_4 removed by each process is also shown. The loss to the stratosphere is the amount of CH_4 transported across the tropopause (one-way transport).

Table 2 Kinetic Isotope effects for the various CH_4 sinks in the troposphere and stratosphere. The strengths of each sink is also included, as well as references for each value. Significant differences in the KIEs from different sources are evident.

CH_4 Sink	Strength, Tg/yr (IPCC-2007)	$\alpha_C = \dfrac{k_{12C}}{k_{13C}}$	$\alpha_H = \dfrac{k_H}{k_D}$	KIE Reference
Losses in Troposphere				
$CH_4 + OH \rightarrow CH_3 + H_2O$	428-511	1.0039±0.0004 1.0054±0.0009	1.294±0.018 1.25±	Saueressig et.al., 2001 Cantrel et.al. 1990 Gierczak, 1997
Aerobic Microbial oxidation (forest and grassland soils)	26-34	1.022±0.004 1.022 and 1.025 1.0181±0.0004 1.0173±0.001	 1.099±0.03 1.066±0.007	Tyler, et.al., 1995 Snover, et.al., 2000 Snover and Quay, 1999
Loss to Stratosphere	30-45			
$CH_4 + OH \rightarrow CH_3 + H_2O$		1.0039±0.0004 1.0054±0.0009	1.294±0.018	Saueressig et.al., 2001 Cantrel et.al. 1990
$Cl + CH_4 \rightarrow HCl + CH_3$		1.0621 ± 0.0004 1.066 ± 0.002	1.474±0.026 1.508±0.041	Tyler, et.al., 2000 Saueressig, et.al., 1995 Saueressig, et.al., 1996
$O\left(^1D\right) + CH_4 \rightarrow CH_3 + OH$		1.013	1.06	Saueressig, et.al., 2001

I.5 Conventional isotopic analysis

Conventional isotopic ratio measurements of CH_4 are made on specially designed isotope ratio mass spectrometers (IRMS). The highest precision $\delta^{13}C$ and δD

measurements reported to date are ± .04 ‰ and ±1‰ (1σ) (Rice et.al., 2001). This level

of precision is sufficient to allow tracking of isotopic ratio changes in the "background"

ambient atmosphere (i.e., far away from sources) Variations in $\delta^{13}C$ and δD, as measured

by Tyler et.al. (2007) show an approximate amplitude of 0.5‰ and 15 ‰, respectively

and inter-hemispheric variations of 0.2‰ and 10‰, respectively (Quay, 1999). Modern

state-of-the-art measurements of atmospheric CH_4 use gas chromatography/isotope ratio

mass spectrometry (GC/IRMS) on 50-100 ml (STP) whole air grab samples and take 20-

30 min per analysis (Rice et.al., 2001). These measurements, however, currently require

on-line sample preparation and large expensive laboratory-based instrumentation. Due to

significant power requirements, size, and weight of IRMS instruments, field-based

measurements are impractical using this methodology.

I.6 Spectroscopic techniques for isotopic analysis

Spectroscopic techniques show promise for providing true *in-situ* measurements

with little sample preparation and faster analyses. Spectroscopic measurement of the CH_4

isotope ratio using various types of absorption techniques began in the 1990's. CH_4 has

fundamental vibrational modes in the 3.3 μm (ν_3=3019 cm^{-1}) and 7.6 μm (ν_4=1311 cm^{-1})

mid infrared (IR) regions, and much of the work was performed in these regions. There

are also CH_4 vibrational overtones of $\nu_2 + 2\nu_3$ ~7500 cm^{-1} and $2\nu_3$ ~6000 cm^{-1} in the near

IR (1.2-1.7 μm), but the absorption in this region is orders of magnitude lower than the

fundamental modes (Hippler and Quack, 2002; Rothman, 2004). Since different

isotopologues of CH_4 will absorb at different frequencies, due to mass effects on the ro-

vibrational modes, a determination of the quantities of $^{13}CH_4$, CH_3D, and CH_4 can be made, and the isotopic ratios can be calculated. However, the precision of recent spectroscopic measurements of isotope ratios at background CH_4 levels was poor for $\delta^{13}C$-CH_4 (±11‰), and δD-CH_4 measurements have only been done on pure CH_4 samples or pre-concentrated samples to achieve reasonable precision. Such data is not sufficient to detect changes in ambient CH_4 and would only roughly characterize sources. The following is a timeline of the research on this subject:

1992: Webster and May (1992) used a tunable diode laser absorption spectrometer (TDLAS) system, known as the Balloon-borne Laser In Situ Sensor (BLISS), to make in-situ stratospheric (altitude of 30-35 km) measurements of CH_4, $^{13}CH_4$ (and thus $\delta^{13}C$), as well as N_2O, and $OC^{18}O$. Their system operated at wavelengths near the ν_4 fundamental, used a long (200m) open path, and used frequency modulation combined with second harmonic detection. A reference cell of CH_4 was used for wavelength calibration, and concentration was determined by comparison with published linestrengths. They measured a $\delta^{13}C$ of -45‰ (close to the the tropospheric background of -47.2‰), but their precision was ±90‰ (at 0.82 ppm CH_4 concentration), making it inadequate for detecting changes in background stratospheric isotope ratios.

1993: The following year, a group at the Max Planck Institute measured $\delta^{13}C$ using a liquid nitrogen-cooled Pb-salt TDLAS operating at the ν_3 fundamental (tuning range ~0.2 cm^{-1}), with a 36 cm single pass absorption cell operated at 23 torr, and

14

temperature controlled to within 0.1 K (Schupp et.al., 1993). They used three absorption cells to simultaneously measure the sample, an isotopic ratio standard, and pure $^{13}CH_4$--allowing them to determine the sample spectra as a combination of the reference and the pure $^{13}CH_4$. The laser was frequency modulated at 40 kHz and a lock-in amplifier used to obtain the 2nd harmonic (2f) signal. They achieved a precision of ±1‰ on samples with concentrations of 25,000 ppm.

1994: Bergamaschi et.al. (1994), from the same Max Planck Institute group improved the TDLAS system with a 1.5 m multi-pass White cell (213 m effective length) for the sample (but kept single pass cells for the reference gases). They also expanded their scope to include δD measurements using pure CH_3D and a second Pb-salt TDLAS laser. The pressure and $^{12}CH_4$ concentration of the sample cell was controlled automatically so that a consistent concentration was maintained (controlled by the addition of N_2). The same 2f technique was used with a modulation frequency of 10kHz. Both the precision and CH_4 concentration limits were improved. The new system achieved a precision of ±0.44‰ for $\delta^{13}C$ (CH_4 concentration in the cell was 50 ppm) and ±5.1‰ for δD (CH_4 concentration in the cell was 2000 ppm).

1997:   Waltman et.al., (1997) consisting of joint work between NIST and the Rice Quantum Institute at Rice University improved on Webster and May's ambient level measurements with a precision of ±44 ‰ (factor of two better), and claimed their precision would be on the same order (±1‰) as Bergamaschi et.al. at comparable concentrations. Their method also involved a multipass cell (18 m

path length) and used a difference-frequency generation scheme with a 806 nm grating-tuned (e.g., Littman configuration) extended cavity diode laser (ECDL) and a Nd:YAG providing 1064 nm wavelength. With this configuration they were able to generate 1 μW of power at the desired wavenumber (3019 cm^{-1}, corresponding to ~3.3 μm), sweeping over a 10 GHz span.

1999: Furthering the work at the Rice Quantum Institute, A. A. Kosterev used a cryogenically cooled mid-infrared (8.1 μm) quantum cascade laser to measure CH_4, $^{13}CH_4$, and CH_3D lines within a 3 cm^{-1} span (laser current scanning) in combination with a 43 cm absorption cell. Their detection limit on CH_4 concentration was approximately 0.5 ppm. For their isotope ratio measurements they used 16.9 torr of CH_4. They do not provide precision values for their isotope ratio measurements, and were only able to obtain a $\delta^{13}C$ value relative to the HITRAN data since they had no independent measurements for the isotope ratio. Due to the limitations of the wavelength of the laser, they could not tune to the maximum intensity CH_4 lines, and had to use lines that were approximately 1/6 of that intensity.

2000: Bergamaschi and others at the Max Planck Institute used their multi-pass cell TDLAS instrument developed in 1993-1994 to make long term (2 years) measurements of δD trends at the Global Atmospheric Watch station at Izaña, Tenerife. Precise measurement of δD using their system required concentrations of approximately 3000 ppm, and therefore collection of large volumes of air samples followed by preconcentration was necessary. The collection system

involved: (1) pressurization of ambient air (heated +5-10K to reduce condensation) accumulated during the nighttime hours over a two-week period; (2) a drying step (at 40°C to further reduce condensation); (3) expansion of dry sample air to STP into two separate 500 L sample bags; (4) at the end of the two-week period, the samples were compressed into aluminum cylinders to a final pressure of ~1700 psig. Prior to the preconcentration, several traps were used to remove contaminant molecules. The preconcentration involved two stages of adsorption of CH_4 onto activated charcoal at 77K followed by desorption at 373K (stage 1) and ~300K (stage 2). Their overall precision (including the errors due to the preconcentration stages) was reported as ±1.0‰.

2001: The highest (reported) precision isotope ratio measurements at ambient concentrations for CH_4 using spectroscopic techniques were made by Dahnke, et.al. (2001), at the Universität Düsseldorf. Their system was the first to implement the cavity ringdown technique, which is the approach we are also using, as explained in Section II. Their measurements were taken on natural air samples (ambient concentration measured to be 1.921 ± 0.011 ppm), using a CO overtone laser electro-optically modulated to generate 10 GHz sidebands with 50 μW of power in the 3.3 μm CH_4 absorption region, and a 50 cm cavity. Their isotope ratio precision was ±11‰, a factor of four (4) improvement over that reported by Waltman four years earlier.

2001: During the same yearm Uehara, et.al. (2001), at Keio University achieved high precision (±0.3‰) $\delta^{13}C$ measurements on pure CH_4 samples. A tunable

semiconductor laser near 1.66 µm (locked using a CH_4 reference cell and a second harmonic stabilization technique) and a multi-pass absorption cell system with a long (100x) pathlength for the $^{13}CH_4$ absorption wavelength, compensated for the lower relative concentration (~1% of $^{12}CH_4$). This enabled them to use the same vibrational mode for both isotopologues, significantly reducing the temperature effects on the relative intensities that occur when the absorption lines have different ground states. Finally, they claim their precision could still be maintained at concentrations as low as 1% CH_4 by increasing the pressure in the cell assuming no interference from other molecules. Their measurement results were obtained using 2 calibrated standards with known $\delta^{13}C$ (from GC-MS measurements), one standard was used as a initial reference, followed by two subsequent measurements of each standard.

2002: Furthering the Uehara work, Yamamoto and Yoshida (2002) improved the precision on pure samples by including measurements of CH_3D concentration (and therefore δD). The improved precision was due to the removal of CH_3D interference on the $^{13}CH_4$ measurement (and vice versa). This required the use of a new cell with longer path length. The final precision on pure CH_4 was ±0.027‰ for $\delta^{13}C$ and ±0.7‰ for δD. In this case, the precision was made using an initial measurement of 2 standards to obtain the correction coefficients, followed by 3-5 measurements of an unknown.

2006: NOAA's Earth System Research Laboratory, NASA's Jet Propulsion Laboratory, Brazil's Instituto Nacional de Metrologica, and NIST (Trudeau, et.al., 2006) used

difference frequency generation similar to that of Waltman et.al. (1997). In addition, they made use of a cryogenic column preconcentration process to measure ambient CH_4 levels, with a concentration enrichment factor of 2540 (CH_4 concentration in the instrument is 4480 ppm) for $\delta^{13}C$ measurements, and 540 times (CH_4 concentration at the instrument is 1020 ppm) for δD measurements. The precision of these measurements was reported as ±12‰ for both $\delta^{13}C$ and δD. Carbon isotope measurement precision required the use of experimentally measured reference cell spectra (as opposed to HITRAN database reference) as part of the experiment in order to "correct for variations in instrument response." The δD measurements did not use the reference cell, and therefore reference the average of all their samples to determine precision.

2008: Los Gatos Research, Inc. introduced a commercially available CH_4 isotope ratio analyzer using an integrated cavity output spectroscopic technique in the near-IR region (1650 nm). According to the specification sheet, the system has a reported ±1‰ precision for $\delta^{13}C$. Although the concentration requirements for that precision are ambiguous, the system requires CH_4 concentrations in the range 200-10,000 ppm, with a 10-second response time. The high concentration requirements limit the applicability of the system to high concentration sources such as hydrothermal vents.

I.7 Motivation

A portable field-deployable instrument capable of detecting small isotopic ratio changes in the background atmosphere as well as near sources and sinks would enable unprecedented measurement campaign capabilities, by providing real-time *in-situ* CH_4 isotope measurements. *In-situ* measurements allow one to immediately detect changes in isotopic composition and collect data more intelligently. These measurements would also allow the tracking of isotopic ratio changes over time, to determine both seasonal changes and long-term trends, and by location to provide "maps" of CH_4 isotopic ratios in the Earth's atmosphere. Since the isotopic ratio indicates the relative effects of sources and sinks, it would provide a large amount of data to improve atmospheric models, and ultimately provide valuable information on their impact on the concentrations of CH_4 in the atmosphere. Airborne measurement campaigns in the free troposphere and stratosphere (e.g., using NASA's ER-2, Global-Hawk, Proteus, or weather balloons) would greatly expand our understanding of CH_4, its sources and sinks, and its effect on the environment. Stratospheric isotope information, in particular, is currently limited due to the difficulty of obtaining air samples, but large-scale measurements would enable better understanding of the effect of stratospheric photochemistry on atmospheric CH_4 (Rice et.al., 2003). Of the above optical techniques, CRD (e.g., Dahnke, 2001) is one of the most promising in terms of sensitivity because (1) it is immune to amplitude noise of the laser, which limits the sensitivity of direct absorption techniques which must measure the input and ouput power of the sample cell, and (2) the high-finesse cavity generates a long effective path length (and therefore the number of molecules the photons can

interact with) which increases the absorption signal. While CRD has the potential to provide advances in instrumentation for isotopic ratio measurements, significant gains in precision must be made before it is useful.

II. Methods

II.1 Experimental approach

CRD spectroscopy uses the exponential decay of light intensity emitted from a high finesse resonant cavity to measure the concentration of gases within the cavity, that absorb at the specific frequency of the circulating light. When the frequency of the laser matches a mode of the cavity, the light intensity inside the cavity (and therefore the signal from an output photodiode at the end of the cavity) increases. At a pre-selected threshold signal level, a feedback circuit shuts off the light going to the cavity, and this initiates the decay (ringdown) of the signal from within the cavity. The output signal $S(t)$—the small fraction transmitted by the output mirror—is proportional to the intensity within the cavity, and is given by:

$$S(t) = S_0 e^{-\beta t} \tag{3}$$

Where S_0 is the level of the detected signal at time $t = 0$, and β is the decay constant ($1/\tau$, where τ is the ring-down time). β can be decomposed into $\beta = \beta_{sample} + \beta_0$, where β_{sample} ($1/\tau_{sample}$) is the contribution from the absorption strength of the sample, and β_0 ($1/\tau_0$) is the background absorption of the light due to mirror transmission, absorption, and scattering, background gases, etc. In theory, β_0 is constant and can be obtained by measuring a ring-down without the sample of interest in the cavity. Subtracting out β_0

22

leaves β_{sample} from which we determine the sample concentration using the Beer-Lambert Law. Typical signal decays corresponding to β_0 and β_{sample} ($^{13}CH_4$ in this example) are shown in Figure 3. Scanning in frequency and determining each decay constant results in an absorption spectrum. Absorption strengths can be obtained by matching absorption to a database such as HITRAN (Rothman et.al., 2005), but empirical measurements using calibration standards of known isotopic ratio improve the accuracy and precision of the measurements. Isotopic ratio measurements only require a stable <u>relative</u> measurement of the concentrations of the isotopologues, but CRDS allows us to obtain $\delta^{13}C$, δD, and CH_4 concentration with the same instrument. For our initial studies we focused on $\delta^{13}C$ over δD due to larger absorption signals resulting from a higher abundance of ^{13}C (~1%) relative to D (~0.08%).
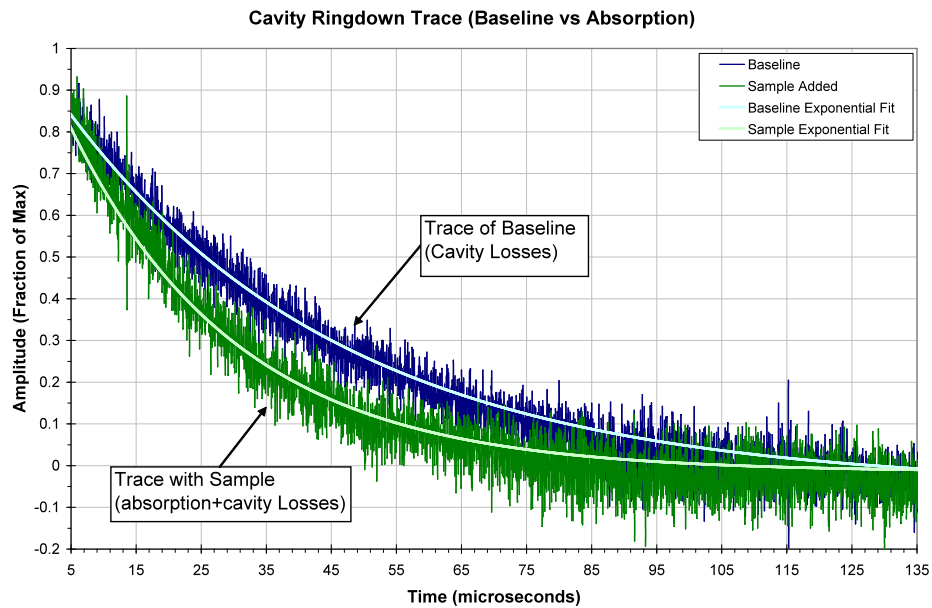
Figure 3 Cavity ringdown traces for a baseline and with an absorbing sample. The exponential fits are obtained using the Fast Fourier Transform components (see Equation **(4)**).

23

While previous efforts at spectroscopy-based isotopic ratio measurements focused mainly on the mid-IR region spectrum for CH_4 (3000-4000 nm, or 2500-3333 cm^{-1}), we used the near-IR region (1280-1340 nm, or 7463-7812 cm^{-1}). This region is attractive from a design standpoint because of the availability of low-cost, robust, and high-resolution tunable diode lasers. It is also attractive from a spectroscopic standpoint because the near-IR is a region with a large number of spectroscopic lines for CH_4, but a small number for other trace atmospheric gases. This is a region of overtone vibrational frequencies, specifically the $\nu_2 + 2\nu_3$ overtone. In this region the spectral line intensities of the major ($^{12}CH_4$) lines are of the order 10^{-22} cm^{-1}/(molec/cm^2). Figure 4 shows a simulation of the spectra for ambient CH_4 and other common atmospheric gases using information from the HITRAN database. We can further reduce contamination effects (due to H_2O, CO_2, O_3, other hydrocarbons, or atmospheric particulate matter) using low temperature traps, chemical adsorbents, and/or filters to pretreat the air sample, if required.
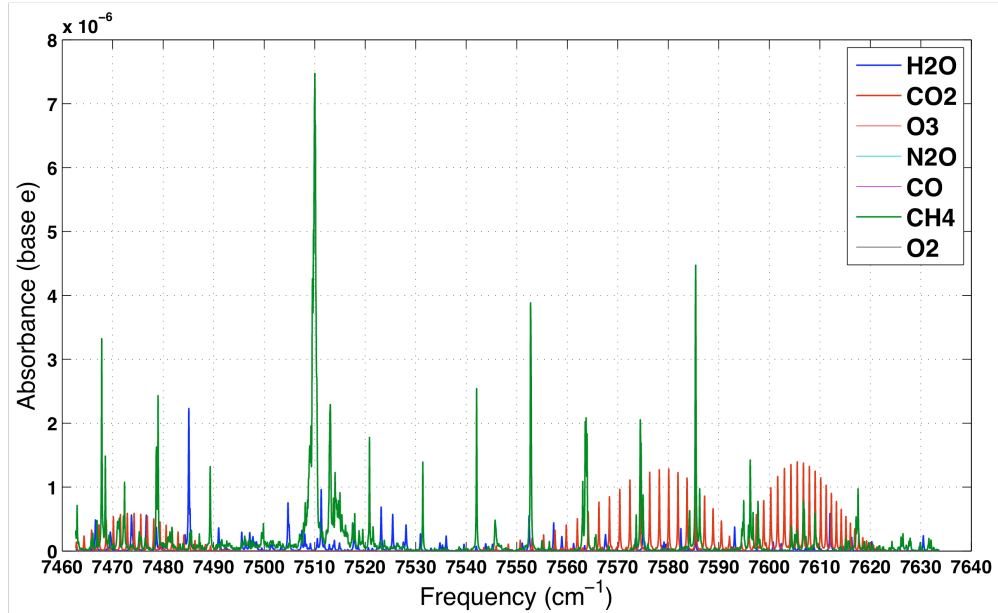
Figure 4: Simulation of the pressure-broadened (760 torr) absorption spectra of the ambient atmosphere (with 1ppm H_2O and all others at their ambient concentrations) using the 2004 HITRAN database. *Green*: CH_4 (1.8 ppm), *blue*: H_2O (1ppm), *red*: CO_2 (383 ppm). Other potenial interferers shown in the legend are too small to be visible. This plot depicts several possible regions where there will not be interference from other gases.

II.2 Experimental setup

The following subsections describe the individual components of our laboratory setup. These components can be seen in the system diagram in Figure 5, and also in the photograph in Figure 6.

Cell/Cavity: The absorption cell (L = 85 cm), consists of a glass tube with inlet and outlet ports, sealed with o-ring compression fittings. Two 2-¾" stainless steel flanges on either end hold the mirrors, with approximately 9 cm of flexible vacuum hose between the mirrors and the glass cell. Each flange/mirror assembly is held in a 2-axis optical mount to enable alignment of the mirrors. The cavity mirrors are 1" concave mirrors (Newport SuperMirrors™, Part #:10CV00SR.60F: nominal reflectivity: R>99.97%;

transmission: T<300 ppm; loss: <100 ppm, r_{curv} = 1 m, λ_0 = 1320 nm). Baseline noise levels in our experiments show a typical cavity loss of 200 ppm/pass, which is less than the total expected mirror losses (800 ppm), and implies a cavity finesse of F >30,000. The free spectral range (spacing between cavity TEM$_{00}$ modes) of a resonant cavity is $FSR = c/(2L)$, so our cavity FSR = 175 MHz (0.0058 cm^{-1}). This determines the minimum step size of our system, assuming only the TEM$_{00}$ mode is excited.

Cavity Tuning: To give truly continuous laser scanning, one of the flange/mirror mount assemblies is attached to a piezo-electric transducer (PZT) translation stage, allowing the cavity length to be modulated over one FSR. Modulating the cavity length ensures that the cavity and laser are mode-matched to achieve resonance at each frequency step. The PZT stage is controlled using a triangle wave from a frequency generator, with a typical frequency of 12 Hz.

Laser: The laser source (New Focus *Velocity* Tunable Diode Laser, Model 6324), provides a coarse tunable range of 1280-1340 nm (0.01 nm resolution), and a fine tuning range of ±0.2 nm (~10 MHz resolution). The fine-tuning is accomplished using a PZT inside of the laser head that changes the mirror tilt angle (a modified Littman-Metcalf configuration), which tunes the laser by smaller increments than the coarse screw drive provides. The resolution is determined by the noise of the applied tuning voltage, with a minimum precision of about 10 MHz. The laser is linearly polarized (900:1 polarization ratio), and has an elliptical beamshape (approximately 3 mm:1 mm at the laser exit aperture).

Beam Shaping: Since the beam profile of the laser is not Gaussian, we focus the beam onto a 100-micron pinhole and re-collimate to improve beam quality, which improves the efficiency of coupling to the cavity.

Laser Tuning: The laser PZT is fine tuned using a Measurement Computing USB-1208FS DAQ module connected to the system computer. Noise levels on this voltage output limited our frequency tuning to approximately 75 MHz. The coarse tuning is performed through GPIB control of the laser.

Frequency Measurement (Etalon and Detector #2): Due to nonlinearities in the fine tuning of the laser, it is necessary to accurately determine the frequency scale. In our setup we use an etalon (FSR = 0.222 cm^{-1}, or 6.66 GHz) and a second photodetector (Thorlabs PDA255). Details of this setup and procedure are given in the analysis section.

HeNe Laser (Alignment): To aid the alignment with the cavity, a HeNe laser (Uniphase, Model 1011) is co-aligned with the IR TDL beam using an optical flat.

Detector #1: The output beam of the cavity is focused onto a New Focus Model 1811 High Speed Photoreceiver, which has a conversion gain of 2.4x10^4 V/W, bandwidth of 10 MHz, a noise voltage of 5.9 mV$_{rms}$ (total noise equivalent power = 0.246 μW$_{rms}$), and has a maximum (linear) input power of 53 μW.

Acousto-Optic Modulator (AOM): In order to record the exponential decay from the cavity output, it is necessary to shut off the beam. A Brimrose Model IPM-400-100-1320 acousto-optic (amplitude) modulator is used. The modulator acts as a switch and attenuates the beam by >15 dB—enough to remove any contribution to the cavity output. The AOM driver (Brimrose FFA-400-B2(400)-F1.2) has a rise time of 3.5 ns, which is

four orders of magnitude faster than the time constant of the cavity (~15-20 μs). The AOM is controlled via a triggering circuit, which compares the cavity output signal to a threshold.

PC (Data Acquistion and Control): The exponential decay signal is captured using a data acquisition card (Gage Applied Sciences, Inc., Model CS8012) mounted in a PC. Custom Labview code collects and processes the cavity output signal, controls and monitors the laser, captures the etalon signal for frequency calibration, and saves the data files for post-processing in Excel and Matlab.

Gas flow System: For system testing, CH_4, $^{13}CH_4$, and $^{12}CH_4$ concentrations in the cell are controlled by the flow rates of the various prepared samples used. Three Tylan mass flow controllers, with different flow ranges, are used: (1) a 0-500 sccm for High Purity N_2 for dilution, (2) 0-300 sccm for controlling a diluted (with N_2) CH_4 standard, and (3) 0-10 sccm for a diluted $^{13}CH_4$ standard, prepared from a 99% $^{13}CH_4$ standard (Sigma-Aldrich). Enrichment of CH_4 is performed by adding (3) to (2), with relative flow rates adjusted to get the desired enrichment. Total CH_4 concentration can be adjusted by adding N_2 to the system. The cell pressure, measured using a Teledyne-Hastings Model 2002 Dual Sensor Vacuum Gauge, is adjusted using a valve in the path to the Edwards two-stage high vacuum rotary vane Pump.
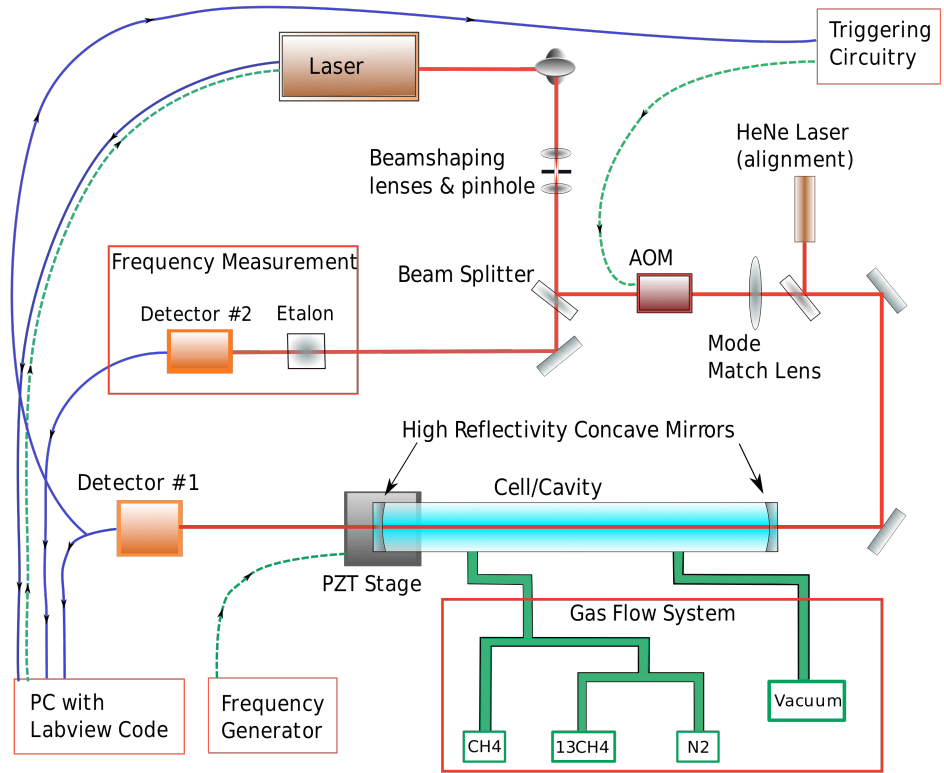
Figure 5 Schematic of our current Cavity Ring Down setup. Discussion of components of CRD system can be found in the text.
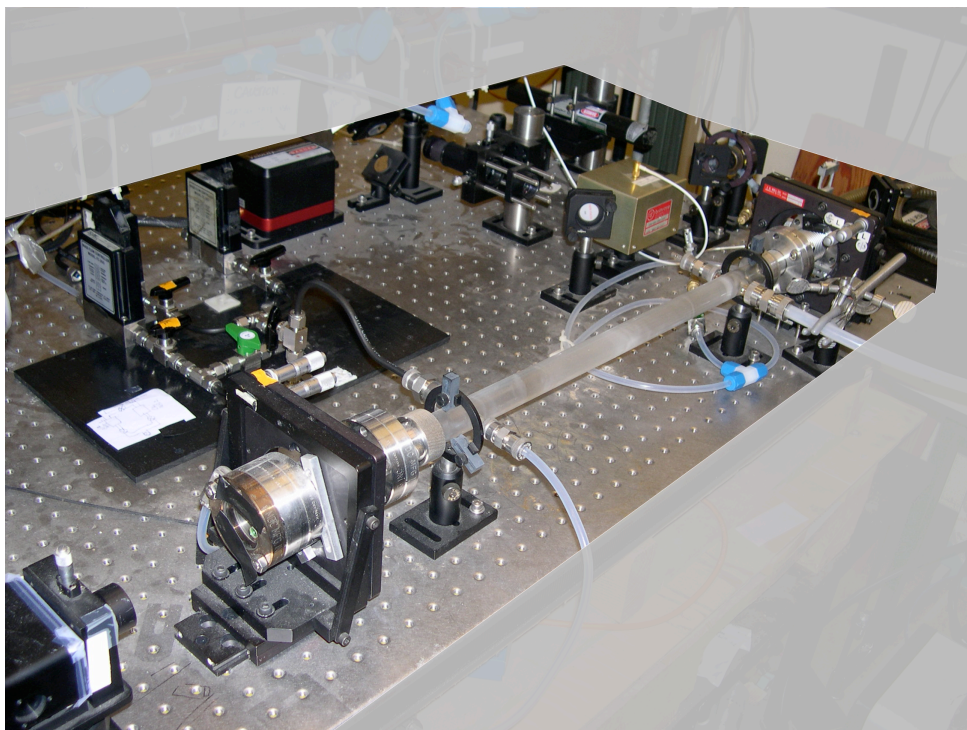
Figure 6 Laboratory setup used for initial studies on the CRD spectroscopy isotope ratio measurements. Photodetector is in the lower left, laser and AOM are in the upper right. Extraneous portions are grayed out for clarity.

II.3 Obtaining absorption spectra

To determine the decay time constant of the ringdown, we have implemented a Discrete Fourier Transform (DFT)-based algorithm (Mazurenka, 2005; Everest and Atkinson, 2008), because the exponential decay constant can be determined (see Equation (4)) from the ratio of the real to the imaginary part of any non-zero frequency component in the Fourier Transform, $X(\omega)$. For the best estimate of β it is desirable to use the component with the maximum SNR, which is typically the first frequency component. When a DFT is used on real (discrete) data, Equation (4) is an approximation

(Everest and Atkinson, 2008), but is sufficiently accurate (<0.1% error) for our current study.

$$\beta = -\omega \frac{\text{Re}(X(\omega))}{\text{Im}(X(\omega))} \tag{4}$$

To determine a decay constant, each ringdown is sampled at 50 MSPS for 4096 points. This is sufficient length (102.4 μs) to capture the entire ringdown event since it is greater than 5 of the (empty) cavity time constants, τ_0. Each data point on the absorption spectrum is then based on an average of 32 of these decay constants. Figure 7 and Figure 8 show our measured spectra for standard CH_4 and $^{13}CH_4$ in the near-IR region for two sets of peaks. Our data compares very well with the simulated spectra using the HITRAN database (shown in red).

The HITRAN database does not contain spectral lines for the isotopologues of CH_4 in the near-IR region. In order to identify these lines, we use 99% pure $^{13}CH_4$ diluted in N_2 and/or zero-grade air. Because sweeping the entire spectral region in high resolution would take an inordinate amount of time, we used the $^{12}CH_4$ lines, the fundamental vibrational frequencies and transition assignments (Hippler and Quack, 2002), to calculate the theoretical vibrational and rotational frequency changes due to isotopic substitution (Herzberg, 1945), and therefore predicted the locations for the $^{13}CH_4$ peaks. This approach is necessary since even the most advanced spectroscopic models (e.g., SpecView from The Ohio State University, and STDS from Institut Carnot de Bourgogne) are not capable of simulating lines in this spectral region. We can calculate

31

the energy levels of the anharmonic oscillator to first order using the correction factors, which have been estimated for CH$_4$, and the following equation (Califano, 1976):

$$E(v_1, v_2, v_3, v_4) = \sum_{i=1}^{4} hc\omega_i\left(v_i + \tfrac{1}{2}\right) + \sum_{i=1}^{4}\sum_{j\geq i} hcx_{ij}\left(v_i + \tfrac{d_i}{2}\right)\left(v_j + \tfrac{d_j}{2}\right) \tag{5}$$

The correction factors, x_{ij}, represent the interaction between the ith and j^{th} vibrational modes, and can be conveniently expressed as elements of a (symmetric) matrix:

$$\ddot{x} = \begin{pmatrix} -64.6 & 0 & -65.0 & 0 \\ 0 & 0 & -15.0 & -11.2 \\ -65.0 & -15.0 & -17.5 & -12.0 \\ 0 & -11.2 & -12.0 & -6.0 \end{pmatrix}$$

Where the values are those reported by Califano (1976). h is Planck's constant, c is the speed of light, ω_i, v_i, and d_i are the harmonic vibration frequency, quantum number, and degeneracy for the ith vibration mode, respectively. The values for ^{12}CH$_4$ and ^{13}CH$_4$ are listed in Table 3, where the ω_i are based on the results from Boudon et.al. (2006). We can then calculate the energies for the ground state $E(0,0,0,0)$ and excited state $E(0,1,2,0)$ using Equation (11), and the wavenumber (in cm^{-1}) for the overtone is then given by

$$\tilde{v} = \frac{1}{hc}\left[E(0,0,0,0) - E(0,1,2,0)\right].$$

Table 3 Fundamental modes of ^{12}CH$_4$ and ^{13}CH$_4$

Vibration Mode	v_1	v_2	v_3	v_4
Symmetry Group	A1	E	F2	F2
Type	Stretch	Bend	Stretch	Bend
Degeneracy	1	2	3	3
Absorption type	Raman	Raman	IR	IR
^{12}CH$_4$ Frequency, ω, cm^{-1}	3143.2	1572.6	3155.0	1364.0
^{13}CH$_4$ Frequency, ω, cm^{-1}	3142.1	1572.8	3145.0	1356.0

Our calculations predict a shift of -19.8 cm^{-1} (+3.5 nm) for the $\nu_2 + 2\nu_3$ overtone due to the substitution of ^{13}C for ^{12}C, and assuming that to first order the entire ro-vibrational spectrum shifts by that amount. Therefore we scanned the regions 15-20 cm^{-1} higher than the two largest peaks in the ^{12}CH$_4$ spectra (1331 nm and 1324 nm). Results of this search are also shown in Figure 7(b) and Figure 8(b) where prominent ^{13}CH$_4$ lines were found 17.0 cm^{-1} (3.0 nm) above their respective ^{12}CH$_4$ lines, which compares well with our estimate (16% error). Further theoretical study to address additional minor isotopic effects should help to resolve the 0.45 nm discrepancy. Note that the theoretical lines in Figure 7(b) and Figure 8(b) are taken from the HITRAN database, and are currently assigned to ^{12}CH$_4$. Therefore, one additional product of this work is the identification of ^{13}CH$_4$ lines for HITRAN. Since the current HITRAN data was obtained using a sample of "standard" CH$_4$ (Brown, 2005) with an unknown isotopic ratio, the exact line intensities for the ^{13}CH$_4$ lines need to be further verified, but agree with the expected ~1.1% relative ^{13}CH$_4$ concentration. This same technique will be applied to obtaining CH$_3$D lines, although the change in the symmetry of the molecule due to a single H to D substitution complicates the calculation of the isotopic shifts.
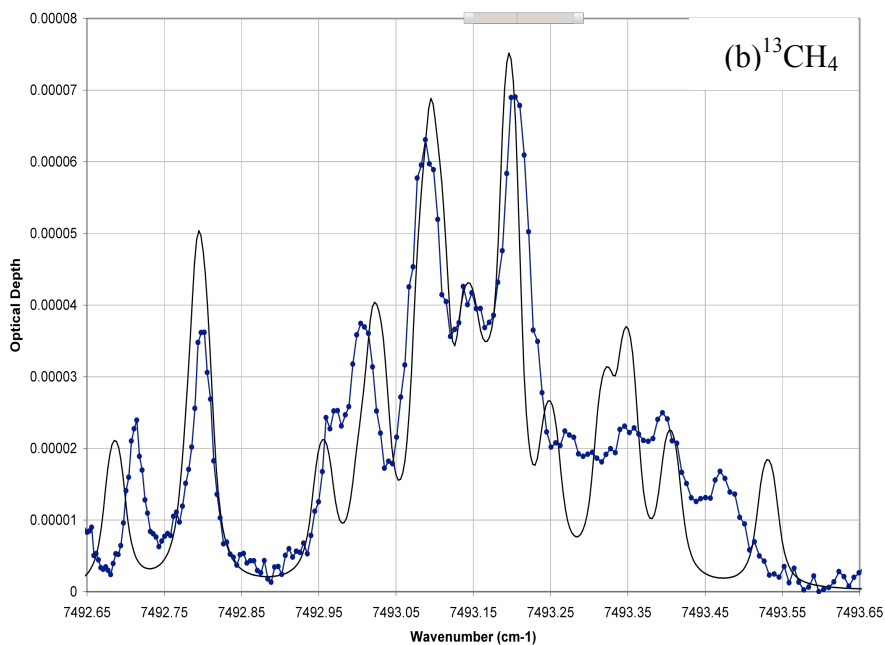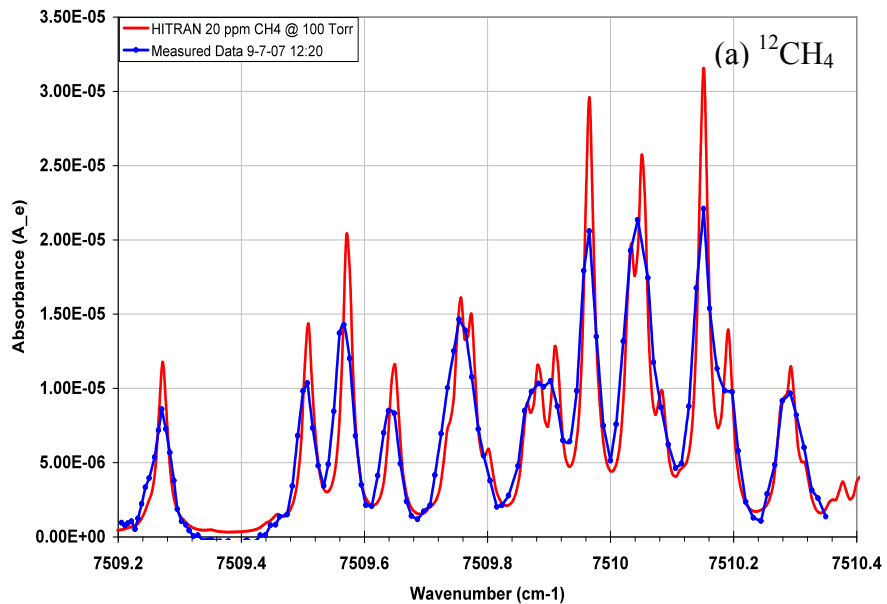
Figure 7 (a) The largest $^{12}CH_4$ spectra for the $\nu_2 + 2\nu_3$ overtone and **(b)** the corresponding and $^{13}CH_4$ spectra isotopically shifted by 17 cm^{-1}. *Blue*: Experimental data from CRD system, *Red*: Theoretical spectra using the HITRAN database. The $^{13}CH_4$ spectra is complicated by overlapping $^{12}CH_4$ lines.
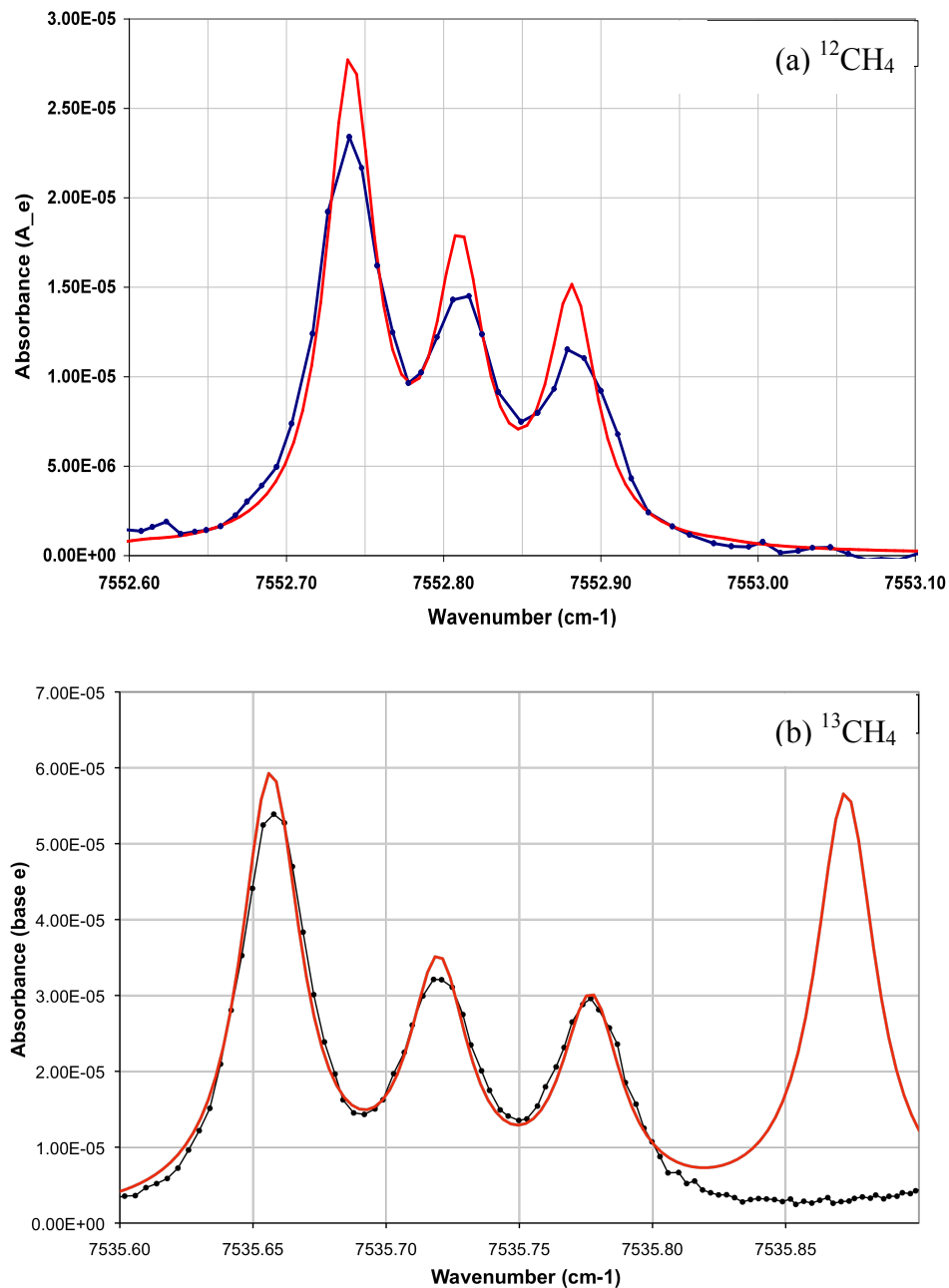
Figure 8 Spectra for **(a)** 20 ppm $^{12}CH_4$ and **(b)** $^{13}CH_4$ for a high absorption triplet showing an isotopic shift of (17 cm^{-1}). *Blue*: Measured data for 20 ppm CH4 and using 99% $^{13}CH_4$; *Red*: Pressure broadened lines from the HITRAN database. The additional peak in (b) at 7535.87 cm^{-1} is a weaker $^{12}CH_4$ line from the database, which enables us to make isotope ratio measurements using a single high resolution scan of the CRDS (~0.8 cm^{-1}).

The highest intensity peaks shown in Figure 7 are about a factor of two times larger than those in Figure 8, but are less suitable for accurate isotope ratio measurement due to the large number of $^{12}CH_4$ and $^{13}CH_4$ which overlap. This makes curve fitting and individual absorption estimates more difficult. On the other hand the peaks shown in Figure 8 show significant separation, and there are three $^{13}CH_4$ peaks and an isolated $^{12}CH_4$ peak. This arrangement makes it much simpler to determine the absorption of $^{13}CH_4$ and $^{12}CH_4$ individually. A large water peak is also observed, but it is possible to reduce that significantly using an H_2O trap into the gas inlet system. Difficulties due to this H_2O peak will be discussed in the Results section.

II.4 Isotope ratio sample generation

Having found suitable $^{13}CH_4$ lines, it was then possible to conduct preliminary isotope ratio measurements on a standard CH_4 and enriched samples. Mixtures of ultra high purity CH_4 (Matheson Tri-Gas) and 99% $^{13}CH_4$ (Sigma-Aldrich) were prepared, with concentrations measured on a GC-FID system operated by the Khalil laboratory here at Portland State University. The CH_4 and $^{13}CH_4$ mixtures had measured concentrations of $[CH_4]_{STD,0} = 1987 \pm 4$ ppm, and $[^{13}CH_4]_{STD,1} = 43.6 \pm 0.2$ ppm. Because this method could only increase the concentration of $^{13}CH_4$, our experiments only represent isotopic enrichment starting at the CH_4 isotope ratio in our standard which was measured to be -38.9‰ using an IRMS. Furthermore, since our system is a dynamic flow system, rather than a static cell design, the ratios of the CH_4 and $^{13}CH_4$ mixtures are controlled using mass flow controllers, which were calibrated using an Alltech Digital Flow Check meter

(Model DFC-HR). The cell inlet and outlet flows were set to obtain a pressure of 110 torr inside the cell for the baseline CH_4 measurement (the addition of $^{13}CH_4$ increased the pressure slightly due to additional inflow, but the outflow was not adjusted). $^{13}CH_4$ enrichments of 1-10% were performed (0.2-2 ppm additional $^{13}CH_4$), which correspond to a $\delta^{13}C$ range of approximately -40‰ to +30‰.

The percent enrichments are calculated by assuming that under steady state conditions the ratios of partial pressures of the gas standards are equivalent to the flow rates into the cell. Starting with the $\delta^{13}C$ of the standard ($\delta^{13}C_{STD,0}$), we obtain the ratio of the concentrations of $^{13}CH_4$ and $^{12}CH_4$ for the standard, $\Delta^{13}C_{STD,0}$:

$$\Delta^{13}C_{STD,0} = \frac{[^{13}CH_4]_{STD,0}}{[^{12}CH_4]_{STD,0}}$$

$$= \frac{[^{13}CH_4]_{PDB}}{[^{12}CH_4]_{PDB}}\left(1 + \frac{\delta^{13}C_{STD,0}}{1000}\right)$$

(6)

where $[^{13}CH_4]_{STD,0}$ and $[^{12}CH_4]_{STD,0}$ are the concentrations of $^{13}CH_4$ and $^{12}CH_4$ for our standard, respectively. These can then be calculated for the standard:

$$\left[^{13}CH_4\right]_{STD,0} = \Delta^{13}C_{STD,0}\left[^{12}CH_4\right]_{STD,0}$$

$$\left[^{12}CH_4\right]_{STD,0} = \frac{\left[CH_4\right]_{STD,0}}{\left(1 + \Delta^{13}C_{STD,0}\right)}$$

(7)

With a $\delta^{13}C_{STD,0}$ = -38.9‰ and a PDB standard ^{13}C ratio of 0.0112372, we obtain $[^{13}CH_4]_{STD,0}$ = 21.28 ppm and $[^{12}CH_4]_{STD,0}$ = 1970.72 ppm. The concentrations of $^{12}CH_4$ and $^{13}CH_4$ inside the cell ($[^{12}CH_4]_{cell}$ and $[^{13}CH_4]_{cell}$, respectively) are then calculated using the relative flow rates of the standards:

$$\left[{}^{12}CH_4\right]_{cell} = \left[{}^{12}CH_4\right]_{STD,0}\left(\frac{f_{CH_4}}{f_{CH_4} + f_{{}^{13}CH_4}}\right) \qquad (8)$$

and

$$\left[{}^{13}CH_4\right]_{cell} = \left(\frac{f_{{}^{13}CH_4}}{f_{CH_4} + f_{{}^{13}CH_4}}\right)\left[{}^{13}CH_4\right]_{STD,1} + \left(\frac{f_{CH_4}}{f_{CH_4} + f_{{}^{13}CH_4}}\right)\left[{}^{13}CH_4\right]_{STD,0} \qquad (9)$$

Where f_{CH4} and $f_{{}^{13}CH_4}$ are the flow rates for the prepared CH_4 and $^{13}CH_4$ gas standards, respectively. The percent enrichment, E, is then:

$$E = \frac{[{}^{13}CH_4]_{cell} - [{}^{13}CH_4]_{STD,0}}{[{}^{13}CH_4]_{STD,0}} \cdot 100 \qquad (10)$$

and, finally, the predicted isotope ratio in the cell, $\delta^{13}C_{cell}$, is:

$$\delta^{13}C_{cell} = \frac{\left(\dfrac{[{}^{13}CH_4]_{cell}}{[{}^{12}CH_4]_{cell}}\right) - \left(\dfrac{[{}^{13}CH_4]_{PDB}}{[{}^{12}CH_4]_{PDB}}\right)}{\left(\dfrac{[{}^{13}CH_4]_{PDB}}{[{}^{12}CH_4]_{PDB}}\right)} \cdot 1000 \qquad (11)$$

The calculations of predicted carbon isotope ratios, using Equation (11), for the two data sets presented in this paper are shown in Table 4.

Table 4 Expected $\delta^{13}C$ for experimental conditions. These are calculated using the equations in the text, based on the flow rates, isotopic composition and concentrations of the CH_4 standards.

	Flow std 1 (13CH4), sccm	Flow std 0 (CH4), sccm	Fraction std 1	Fraction std 0	[13CH4] std,ppm	[13CH4] added,ppm	% Enriched	[13CH4]/[12CH4] cell	Predicted $\delta^{13}C$ cell
14-Oct-08	0.0	104.2	0	1	21.284	0	0	0.0108001	-38.9
	1.0	104.2	0.0095	0.9905	21.082	0.41407	1.95	0.0110122	-20.0
	1.6	104.2	0.0151	0.9849	20.962	0.65875	3.10	0.0111395	-8.7
	2.6	104.2	0.0243	0.9757	20.766	1.06045	4.98	0.0113516	10.2
	3.7	104.2	0.0343	0.9657	20.554	1.49372	7.02	0.0115849	30.9
17-Oct-08	0.0	104.2	0	1.0000	21.284	0.00000	0.00	0.0108001	-38.9
	0.5	104.2	0.0048	0.9952	21.182	0.20802	0.98	0.0109061	-29.5
	2.0	104.2	0.0188	0.9812	20.883	0.82034	3.85	0.0112243	-1.1
	3.0	104.2	0.0280	0.9720	20.688	1.21903	5.73	0.0114365	17.7

II.5 Frequency calibrations

To obtain the high-resolution absorption spectra for these experiments, we use the fine-tuning mode of the TDL laser. Unfortunately, this tuning is not linear with the applied voltage, and does not remain constant. It is more linear in the middle of the tuning range, and becomes less so as you approach the extremes of the tuning range. Thus it is desirable to center the spectra in the tuning range. However, due to longer-term drifts in the laser wavelength, over the course of several gas samples (several hours), the spectra will tend to drift towards one extreme or another.

External calibration of the frequency is therefore required. In our configuration we use an etalon with a FSR of $\Delta\tilde{v}_{FSR} = 0.222$ cm^{-1} (6.66 GHz). This means 38 of our cavity modes are within one FSR of the etalon. The etalon is uncoated glass, giving it a reflectivity of $R \approx 3.5\%$ (Best fit estimates $R = 3.378\%$). At this low reflectivity the etalon exhibits a nearly sinusoidal shape for the output amplitude, A_{et}, but the exact form is well known (Tammela, 1997). The frequency scale for our scans, as a function of applied voltage, is obtained using a nonlinear fit, based on the theoretical etalon transmission function, to the etalon output:

$$\hat{A}_{et}\left(\tilde{v}(V_{app}), A_{et,0}(V_{app})\right) = O(V_{app}) + \frac{A_{et,0}}{1 + \dfrac{4R}{(1-R)^2}\sin^2\left(\dfrac{\pi\tilde{v}(V_{app})}{\Delta\tilde{v}_{FSR}}\right)} \tag{12}$$

$$\tilde{v}(V_{app}) = \sum_{i=0}^{5} b_i V_{app}^i$$

$$O(V_{app}) = \sum_{i=0}^{2} a_i V_{app}^i$$

where $\hat{A}_{et}$ is the estimate of the etalon output voltage, A_{et}, R is the reflectivity of the mirrors, V_{app} is the voltage applied to the laser for frequency control, $\Delta\tilde{\nu}_{FSR}$ is the FSR of the etalon, $O(V_{app})$ is a 2nd order polynomial (with coefficients a_i) for the amplitude offset and laser power drift, $\tilde{\nu}(V_{app})$ is a 5th order polynomial (with coefficients b_i) for the frequency, and $A_{et,0}$ is a scaling factor. After the fit to the measured etalon output, the function $\tilde{\nu}(V_{app})$ then provides the frequency scale for the acquired absorption spectrum.

A comparison of the modeled etalon output, using Equation (12), and the measured etalon output using the frequency calibration $\tilde{\nu}(V_{app})$ is shown in Figure 9. In our experiments, the etalon output is measured prior to each ringdown (4096 points sampled at 25 ksps), and the frequency is calculated based on the average during all the ringdowns at that frequency setting. Known frequencies for the absorption peaks (from the HITRAN database, e.g.) can provide the absolute frequency reference; however, for our measurements, the exact location of the peaks is unimportant.
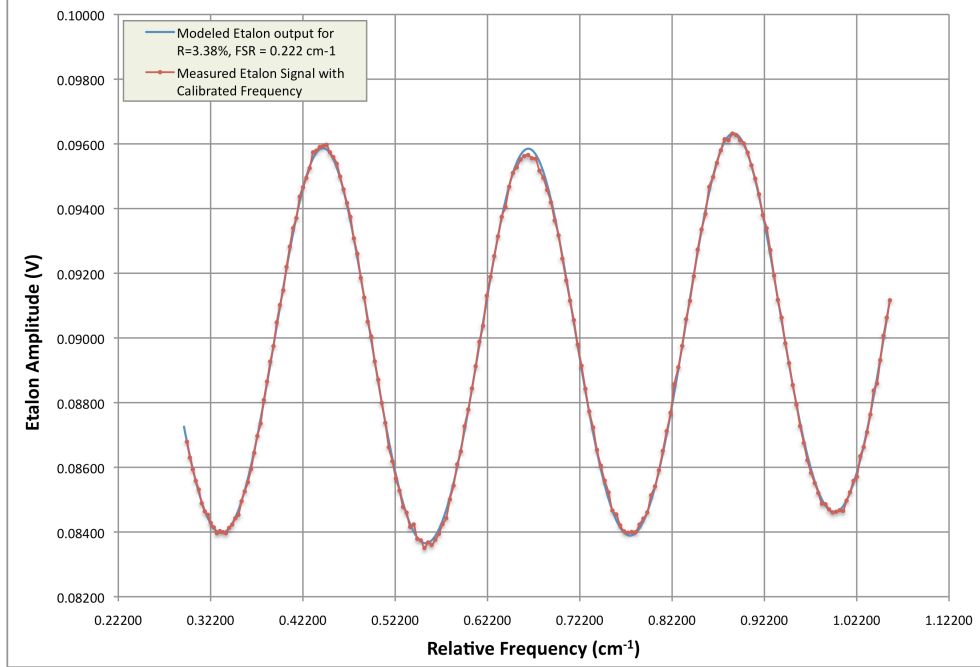
Figure 9 Etalon calibration results showing the corrected frequency (x-axis) and the modeled etalon output. *Red, circles*: measured etalon output is shown, *blue* modeled etalon output for R = 3.378%

II.6 CH$_4$ concentration determination

For our initial study, in order to determine the relative concentrations of ^{12}CH$_4$ and ^{13}CH$_4$, we fit a Lorentzian lineshape to the measured peaks (e.g., Figure 8) using a nonlinear fit routine written in Matlab (R2009a, V7.8, The Mathworks, Inc.). From the fit parameters we can immediately obtain a value that is proportional to the concentration, and can therefore accurately determine relative changes in concentration of the isotopologues. Following the HITRAN documentation (Rothman, 1996):

(13)

$$A_e(\tilde{\nu}) = A_{e,pk} \frac{\gamma^2}{\gamma^2 + (\tilde{\nu} - \tilde{\nu}_0)^2} = A_{e,pk} \pi \gamma \cdot f(\tilde{\nu}, \tilde{\nu}_0)$$

41

$$f(\tilde{v},\tilde{v}_0) = \frac{1}{\pi} \frac{\gamma}{\gamma^2 + (\tilde{v} - \tilde{v}_0)^2} \tag{14}$$

$A_{e,pk}$ is the peak absorbance of for that peak, $\tilde{v}_0$ is the wavenumber of the center of the peak (cm^{-1}), $A_e(\tilde{v})$ is the absorbance at wavenumber $\tilde{v}$, and γ is the linewidth (half-width at half-maximum, in cm^{-1}). $f(\tilde{v},\tilde{v}_0)$ is the normalized Lorentz lineshape (1/cm^{-1}), which has the property that it is unity at the peak, (i.e., $f(\tilde{v}_0,\tilde{v}_0) = 1$). Equation (13) is used to find the parameters that minimize the mean-square error. Because of potential errors in our frequency scale, we calculate the error in both the frequency (using an inverse Lorenztian function) and the absorbance axes, as:

$$MSE = \frac{1}{N} \sum_{i=1}^{N} \left[\frac{1}{\sigma_A^2} \left(A_{e,i} - \hat{A}_{e,i} \right)^2 + \frac{1}{\sigma_v^2} \left(v_{e,i} - \hat{v}_{e,i} \right)^2 \right] \tag{15}$$

$$\hat{v}_{e,i} = v_0 \pm \sqrt{\frac{A_{e,pk} \gamma^2}{A_{e,i}} - \gamma^2} \tag{16}$$

Where the data for the peak are the $i=1..N$ points $(v_{e,i}, A_{e,i})$, $\hat{A}_{e,i}$ is the estimated absorbance at $v_{e,i}$ using the Lorentizian function, $\hat{v}_{e,i}$ is the estimated frequency for $A_{e,i}$ using the inverse Lorentzian shown in Equation (16), and σ_A^2 and σ_v^2 are the variances of the absorbance and the frequency, respectively, which are used to normalize the error in each dimension. The fit parameters are the peak height ($A_{e,pk}$), the half-width at half-maximum linewidth (γ), and the center frequency (v_0). The spectral line intensity, S, scaled by the concentration, c (molec/cm^3), and the path length, L (cm), is equal to the integral of the Lorentzian, which is $A_{e,pk}\pi\gamma$, as shown in Equation (17).

$$c(LS) = A_{e,pk}\pi\gamma \qquad\qquad (17)$$

It is possible to determine the concentration directly using the spectral line intensities from the HITRAN database—however our initial interest is only in changes from the standard, so that proportionality is sufficient. Moreover, without knowing the exact isotopic ratio of the CH_4 used to obtain the HITRAN data, the true spectral line intensity of the $^{13}CH_4$ lines we found cannot be accurately known. The fit algorithm is applied to each peak individually, treating everything else as the background. In this case the background consists of the contributions of the other peaks present in the spectra. Prior to fitting the peak of interest, the background peaks are also fit using a Lorentz lineshape function, and those portions below the peak of interest are subtracted. Once all the background peaks are removed, a final non-linear fit is performed on the peak of interest. This final fit involves varying each initial condition and selecting the parameters corresponding to minimum error. This helps to ensure our fit is not due to a local minimum near our initial condition.

III. Results and discussion

Using the procedure described in the previous section, the concentration change of both $^{13}CH_4$ and $^{12}CH_4$ can be calculated. Figure 10 shows the results for a typical scan, which uses the data from 17 Oct with a predicted enrichment of 0.99% to a $\delta^{13}C$ of -37.9‰ (See Table 4). A scan usually requires about 45 minutes to acquire approximately 250 data points, including system configuration. The green circles in the figure represent the measured absorbance data for this scan. Peak A (the $^{13}CH_4$ peak, which is the same as Peak A shown in Figure 8(b)) is the peak of interest for which the background will be subtracted. First, an estimate of Peak A is subtracted to leave the background peaks. The data points for one background peak are selected and a Lorentzian fit is subtracted from the raw data. This process is repeated until all background peaks are removed. In the figure, the black dashed line represents the total background. The non-linear portion below Peak A shows the advantage of this background subtraction to a more typical linear baseline subtraction as it will produce a more symmetric resultant lineshape. After the background is subtracted a final Lorentzian fit is applied to Peak A, and consists of the 14 data points shown with red circles). The final best fit is shown as the red solid line, and its parameters are used to determine the concentration using Equation (17). The MSE for the fit from Equation (15) is 0.118, the mean square error for just the absorbance (y-axis only) is 4.5e-13, and the area under the Lorenztian curve (proportional to concentration) is 1.005e-6. If we assume a near-background isotope ratio of 0.011 for the HITRAN lines, the true spectral line intensity is 1.69e-22 $cm^{-1}/(molec/cm^2)$. Using this

44

intensity, pressure, cell length, and area under the curve we obtain a concentration of $^{13}CH_4$ of 20.6 ppm, which agrees with the predicted concentration in Table 4 of 21.2 ppm. The blue line in Figure 10 is the sum of the background fit and the peak fit which, as expected, matches closely with the measured data.
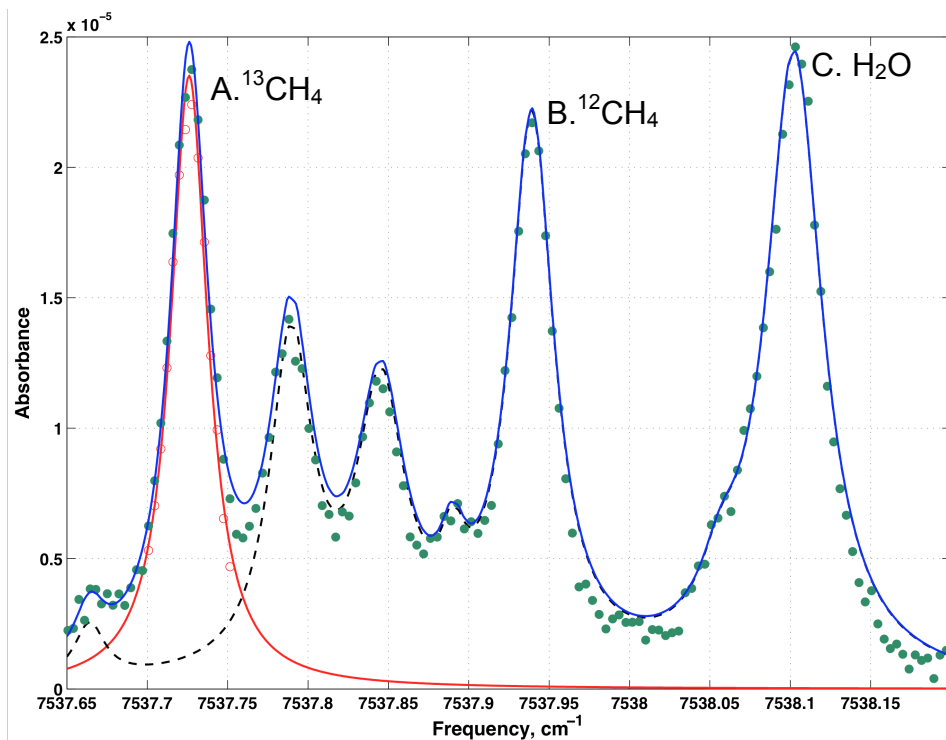
Figure 10 A typical scan showing Lorentzian line fit with background subtraction for the $^{13}CH_4$ peak (Peak A). *Green circles*: Measured CRD spectra; *Black, dashed*: Background for $^{13}CH_4$ peak; *Red dash*: Lorentzian fit to $^{13}CH_4$ peak (Peak A) with background subtracted; *Blue*: combination of Lorentzian fit and background. Peak C is an H_2O line which makes a significant contribution to the background of the $^{12}CH_4$ peak (Peak B).

In our experiment there were contributions from an H_2O line (Peak C) that, due to a small leak on the inlet system, varied significantly over the course of the experiment. We could not correct for all of the H_2O interference on the $^{12}CH_4$ peak and this caused

the $^{12}CH_4$ peak to fluctuate more than expected. Temperature effects may also have contributed to these variations, and will be discussed below. Therefore we made the assumption that the $^{12}CH_4$ concentration was constant, and considered only the change in the $^{13}CH_4$ peak (from our un-enriched CH_4 standard) when calculating $\delta^{13}C$.

We measured spectra for a each of the trials described in Table 4, plus a spectra of the unenriched standard for each day. Analysis similar to that shown in Figure 10 was repeated for each trial, and the $\delta^{13}C$ for each trial was calculated. The results for both datasets are shown in Figure 11 and Figure 12. The plot of measured versus predicted $\delta^{13}C$ shows high linearity, with $R^2 > 0.99$ for both data sets. Thus, the system is linear over a $\delta^{13}C$ range of ~90‰ which encompasses the range of isotopic values of CH4 sources on Earth. The current precision of our measurements can be estimated by the standard error of the linear and results in a precision of ±3.9‰ and 5.6‰. Though insufficient to measure small changes in $\delta^{13}C$ in the air, these results indicate that this approach could be useful for field measurements of CH_4 sources where concentrations are well above ambient levels (e.g., hydrothermal systems, anoxic sediments).
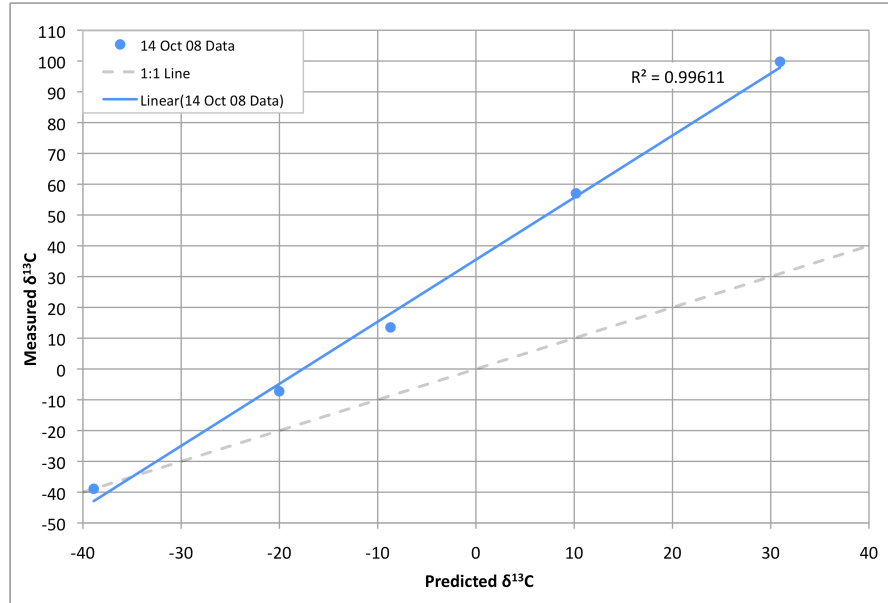
Figure 11 $\delta^{13}C$ enrichment results for 14 October 09 (details listed in **Table 4**), along with a linear best-fit. The best-fit line has a slope of 2.0, and an $R^2 = 0.996$.
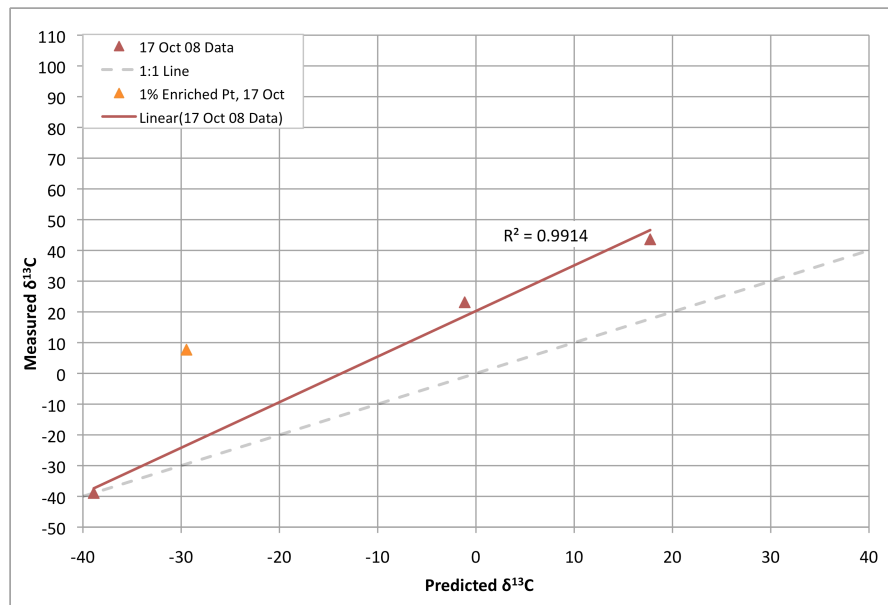
Figure 12 $\delta^{13}C$ results for 17-Oct (details listed in **Table 4**). The data point for 1% enrichment was determined to be unreliable in its predicted $\delta^{13}C$ of -30 ‰ (see text), and therefore was omitted for the linear fit. The best-fit line has a slope of 1.5 and an $R^2 = 0.991$.

The results in Figure 11 and Figure 12 show that there are issues with the performance of the system. First, as previously mentioned, the $^{12}CH_4$ line strength varied significantly, and we were not able to use it to calculate the $^{12}CH_4$ concentration. Our data showed an inter-day difference of averages of 1.7%, normalized standard deviations in $^{12}CH_4$ intensity for the two days of 3.3% and 4.9%, and a change in the ratio of the baseline intensities for $^{13}CH_4$ to $^{12}CH_4$ of 5.3% between the two datasets. Also, the datasets exhibit significantly different slopes (1.5 for 17-October and 2.0 for 14-October) despite the fact that the experimental conditions (flow rates, cell pressure, and gas standards) were the same. These variations most likely resulted from (1) residual errors in frequency scaling between the data sets—which affect the linewidths used to calculate the line intensity using Equation (17), (2) shifts in the background decay constant, β_0, which affects the baseline $^{13}CH_4$ value used to calculate the $\delta^{13}C$, (3) errors in the flow rates for enrichment of the CH_4, either through mass flow controller problems or a leak in the gas inlet system, (4) contaminant molecules such as H_2O or CO_2 interfering with the $^{13}CH_4$ lines, and/or (5) temperature dependent absorbance effects. The last two items are discussed in more detail in the next sub-sections.

There is one final issue concerning the 17 October dataset, and that relates to the datapoint corresponding to a predicted value of -30‰ $\delta^{13}C$, which is a 1% enrichment of $^{13}CH_4$ (see Figure 12, and Table 4). This datum provided a measured $\delta^{13}C$ value approximately 30‰ higher than predicted, roughly 6 standard deviations outside of the best fit regression produced by the other three data and was removed from the analysis.

Though it is included in Figure 12, there are two reasons why this point was excluded. First, the 1% enrichment measurement was made after the highest enrichment of 6% enrichment measurement was performed, which is atypical for these analyses. Since the time interval between the 6% enrichment and the 1% enrichment was less than 15 minutes, it is likely that there was significant residual $^{13}CH_4$ in the system during the 1% scan to cause the value to be enriched. Second, a 1% enrichment required a 0.5 sccm flow rate, which is somewhat below the lower limit of the linear range of the mass flow controller (note that for the 14 October experiment, this low flow regime was not attempted). Thus the actual flow rate was likely higher than the target 0.5 sccm, and would again increase the actual $\delta^{13}C$ measured inside the cell.

III.1 Interference of other molecules

Analysis of the effects of the spectral interference on our measurements revealed that the only significant H_2O line was the large peak 0.2 cm^{-1} higher than the $^{12}CH_4$ peak, while the CO_2 line in the region has an intensity 3 orders of magnitude below that of CH_4, as shown in Figure 13. The largest CO_2 peak is shown in the figure, and those not shown are at least another order of magnitude smaller. According to the HITRAN database, other potential absorbers in this region are NO and OH, but their intensities are at least 25 orders of magnitude below CH_4, and with concentrations well below CH_4 they would not contribute. Therefore H_2O and CO_2 do not seem to be affecting the $^{13}CH_4$ peak. However, the water peak likely did contribute to the variations in the $^{12}CH_4$ peak, as it the H_2O line intensity was found to vary by 20% during the course of the experiment on 14 October. This water contamination was traced to a leak in the inlet system, but computer hardware

and DAQ problems prevented us from re-investigating this issue. The inclusion of a trap to reduce the water concentration seems prudent for future experiments. Several smaller peaks that are evident in the experimental spectra (see Figure 10) are unidentified at this point and are from other contaminants species (e.g., non-methane hydrocarbons).
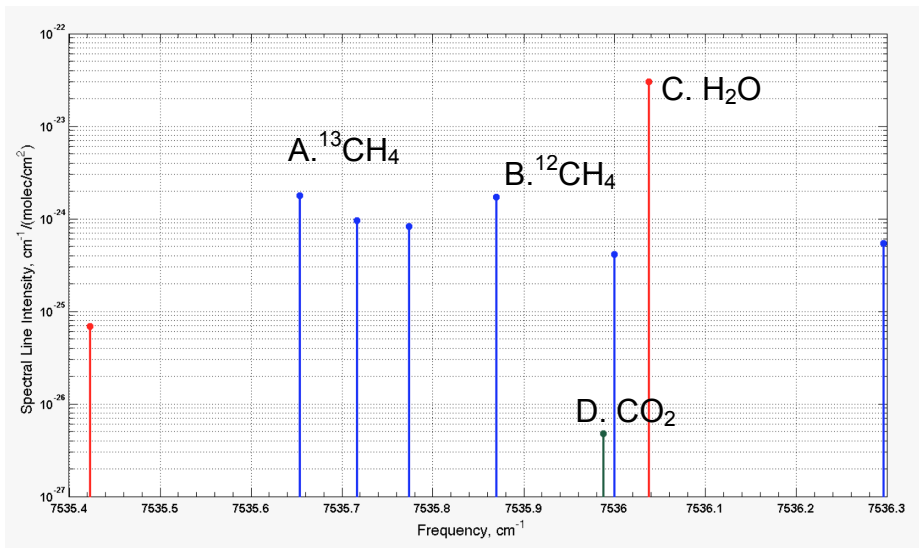
Figure 13 Spectral lines from the HITRAN database for *blue*: CH_4 (Peaks A and B), *red*: H_2O (Peak C) and *green*: CO_2 (Peak D), for the spectral region for **Figure 10** and **Figure 8**(b), with the corresponding peaks labeled consistently.

III.2 Temperature Dependence

Spectral line intensities have a temperature dependence, which results from changes in the population densities of the molecular energy states with temperature. Since the cell temperature varied with the ambient room temperature, we assume fluctuations on the order of 1 K. Line intensity is proportional to the ratio of the population densities of the initial and final states of the transition (Rothman, 1996):

50

$$\frac{S(T)}{S(T_{ref})} = \frac{Q(T_{ref})}{Q(T)} \exp\left(-c_2 E_\eta\left(\frac{1}{T} - \frac{1}{T_{ref}}\right)\right) \frac{\left[1 - \exp\left(\frac{-c_2 v}{T}\right)\right]}{\left[1 - \exp\left(\frac{-c_2 v}{T_{ref}}\right)\right]} \tag{18}$$

Here $c_2 = hc/k = 1.4388$ cm·K, T_{ref} is the temperature corresponding to S listed in the HITRAN database, E_η is the ground state energy for the transition, v is the wavenumber of the transition, and $Q(T)$ is the total internal partition function for energy levels E_i at temperature T:

$$Q(T) = \sum_i e^{\frac{-E_i}{kT}} \tag{19}$$

Since we used only the $^{13}CH_4$ peak (Peak A) for determining $\delta^{13}C$, the temperature dependence does not depend on the relative temperature dependence of the two lines, as is typical in spectroscopic techniques, but only on the $^{13}CH_4$ peak. Gamache et. al. (2000) approximated $Q(T)$ with a 3rd order polynomial for many of the molecules of atmospheric interest:

$$Q(T) = A + BT + CT^2 + DT^3 \tag{20}$$

With the following coefficients for $^{13}CH_4$: A = -52.956, B=2.3113, C=0.0053659, D=0.30232x10^{-5}. The transition for the major $^{12}CH_4$ transition in Figure 8(a) is known and the ground state energy $E_\eta = 62.87$ cm^{-1} (Hippler, 2002). There is a small change in ground state energy between $^{12}CH_4$ and $^{13}CH_4$ (as discussed in Section I.2), but it will not have a significant impact on the temperature dependence. Using this value for the ground state energy in Equation (18), we calculate an estimated temperature dependence on the

[13]CH$_4$ spectral line intensity of 0.43%/K. This suggests that the day-to-day change in temperature would account for less than a 0.5% change in the slope for a 1 K change in temperature, and a 20‰ shift in the intercept value (less critical). Furthermore, a linear variation (constant increase or decrease) of 1 K in temperature over the course of the experiment would only result in a 0.3% change in the slope with only a 1‰ shift in the intercept. Therefore, we conclude that the temperature dependence does not seem to be the major contributor to the slope variation and cannot alone account for the differences observed between October 14 and October 17 results.

We next considered the variations in the [12]CH$_4$ line intensity (Peak B in Figure 10), which prevented us from using it to calculate the δ^{13}C. Since the spectral line intensity of the [12]CH$_4$ must be ~1% of the spectral line intensity, the ground state energy (and thus the temperature dependence) could be significantly different from that of the major lines used for [13]CH$_4$, but since this particular line has not been assigned, the ground state energy is unknown. As an example of the potential magnitude of the temperature dependence, we used a value of 2%/K dependence for the [12]CH$_4$ line-strength in our experiments, which applies to similar *relative* linestrengths at 3.3 μm fundamental mode (Bergamaschi, 1994; Trudeau, 2006). In this case, a 1 K temperature variation could account for at least a significant portion of the 3-5% changes observed in our data, and explain why we could not use the [12]CH$_4$ spectral lines to accurately determine δ^{13}C.

IV. Conclusion

Here we presented new cavity ringdown spectroscopic measurements of the isotopic ratio of CH_4 using a previously unused overtone band in the near-IR region at 7536 cm^{-1}, that exhibits minimal interference from other molecules. We identified a set of strong $^{13}CH_4$ lines that had previously been assigned to $^{12}CH_4$. These were close enough to a single weak $^{12}CH_4$ line to enable (in principle) concentration measurements of both isotopologues in a single, high-resolution scan. We were able to achieve a precision of ±4‰, and our results shows high linearity ($R^2 > 0.99$) over a wide range of isotope ratios. Our precision can be achieved despite the observed long-term changes in slope by performing a two-point calibration prior to the measurement. The optimal frequency of this calibration would be determined empirically. The exact causes of the variations in the slope of the datasets are still unknown. In comparison to other spectroscopic techniques, our prototype has a precision within a factor of 5 of the commercial Los Gatos instrument. However, our instrument operates in a spectral region with a spectral line intensity an order of magnitude lower. We expect that improvements such as temperature stability and removal of contaminant molecules will improve the precision, and produce more consistent calibration curves.

V. References

D. Atkinson. Solving chemical problems of environmental importance using cavity ring-down spectroscopy. *The Analyst*, 128(2):117–125, 2003.

P. Bergamaschi, M. Braünlich, T. Marik, and C. Brenninkmeijer. Measurements of the carbon and hydrogen isotopes of atmospheric methane at izana, tenerife: Seasonal cycles and synoptic-scale variations. *Journal of Geophysical Research-Atmospheres*, 105 (D11).

P. Bergamaschi, M. Schupp, and G. Harris. High-precision direct measurements of $^{13}CH_4/^{12}CH_4$ and $^{12}CH3D/^{12}CH_4$ ratios in atmospheric methane sources by means of a long-path tunable diode laser absorption spectrometer. *Applied Optics*, 33(33):7704–7716, 1994.

J. Bigeleisen and M. Wolfsberg. Theoretical and experimental aspects of isotope effects in chemical kinetics. *Adv. Chem. Phys*, 1:15–76, 1958.

D. Boone. "Chapter 4: Biological Formation and Consumption of Methane," *Atmospheric methane: its role in the global environment*, 2000.

V. Boudon, M. Rey, and M. Loëte. The vibrational levels of methane obtained from analyses of high-resolution spectra. *Journal of Quantitative Spectroscopy and Radiative Transfer*, 98(3):394–404, 2006.

P. Bousquet, P. Ciais, J. Miller, E. Dlugokencky, D. Hauglustaine, C. Prigent, G. Van der Werf, P. Peylin, E. Brunke, C. Carouge, et al. Contribution of anthropogenic and natural sources to atmospheric methane variability. *Nature*, 443(7110):439–443, 2006.

L. Brown. Empirical line parameters of methane from 1.1 to 2.1 μm. *Journal of Quantitative Spectroscopy and Radiative Transfer*, 96(2):251–270, 2005.

S. Califano. *Vibrational States*. John Wiley & Sons, New York, 1976.

C. Cantrell, R. Shetter, A. Mcdaniel, J. Calvert, J. Davidson, D. Lowe, S. Tyler, R. Cicerone, and J. Greenberg. Carbon kinetic isotope effect in the oxidation of methane by the hydroxyl radical. *Journal of Geophysical Research-Atmospheres*, 95(D13).

T. Coplen. Reporting of stable hydrogen, carbon, and oxygen isotopic abundances. *Geothermics*, 24(5-6):707–712, 1995.

H. Dahnke, D. Kleine, W. Urban, P. Hering, and M. Mürtz. Isotopic ratio measurement of methane in ambient air using mid-infrared cavity leak-out spectroscopy. *Applied Physics B: Lasers and Optics*, 72(1):121–125, 2001.

J. De Laeter, J. Böhlke, P. De Bievre, H. Hidaka, H. Peiser, K. Rosman, and P. Taylor. Atomic weights of the elements: Review 2000. *Pure Appl. Chem*, 75(6):683–800, 2003.

E. Dlugokencky, S. Houweling, L. Bruhwiler, K. Masarie, P. Lang, J. Miller, and P. Tans. Atmospheric methane levels off: Temporary pause or a new steady-state. *Geophys. Res. Lett*, 30(19):1992, 2003.

M. Everest and D. Atkinson. Discrete sums for the rapid determination of exponential decay constants. *Review of Scientific Instruments*, 79:023108, 2008.

B. Fawcett, A. Parkes, D. Shallcross, and A. Orr-Ewing. Trace detection of methane using continuous wave cavity ring-down spectroscopy at 1.65 μm. *Physical Chemistry Chemical Physics*, 4(24):5960–5965, 2002.

R. Gamache, R. Hawkins, and L. Rothman. Total internal partition sums in the temperature range 70-3000 k: atmospheric linear molecules. *Journal of molecular spectroscopy*, 142:205–219, 1990.

R. Gamache, S. Kennedy, R. Hawkins, and L. Rothman. Total internal partition sums for molecules in the terrestrial atmosphere. *Journal of Molecular Structure*, 517(1):407–425, 2000.

T. Gierczak, R. Talukdar, G. Herndon, G. Vaghjiani, A. Ravishankara, Journal of Physical Chemistry A. 101: 3125.

G. Herzberg. Molecular spectra and molecular structure. vol. 11. *D. Van Sostrand Co., Inc., Princeton, New Jersey*, page 421, 1945.

M. Hippler and M. Quack. High-resolution fourier transform infrared and cw-diode laser cavity ringdown spectroscopy of the $\nu_2+ 2\nu_3$ band of methane near 7510 cm^{-1} in slit jet expansions and at room temperature. *Journal of Chemical Physics*, 116(14):6045–6055, 2002.

IPCC. *Climate Change 2007: The Physical Science Basis. Contribution of Working Group I to the Fourth Assessment Report of the Intergovernmental Panel on Climate Change*. Cambridge University Press, Cambridge, United Kingdom and New York, NY, USA, 2007.

S. Kassi, B. Gao, D. Romanini, and A. Campargue. The near-infrared (1.30–1.70 μm) absorption spectrum of methane down to 77 K. *Phys Chem Chem Phys*, 10:4410, 2008.

A. Kosterev, R. Curl, F. Tittel, C. Gmachl, F. Capasso, D. Sivco, J. Baillargeon, A. Hutchinson, and A. Cho. Methane concentration and isotopic composition measurements with a mid-infrared quantum-cascade laser. *Optics letters*, 24(23):1762–1764, 1999.

K. Lassey, D. Lowe, and M. Manning. The trend in atmospheric methane $\delta^{13}C$ and implications for isotopic constraints on the global methane budget. *Global Biogeochemical Cycles*, 14(1), 2000.

M. Mazurenka, R. Wada, A. Shillings, T. Butler, J. Beames, and A. Orr-Ewing. Fast fourier transform analysis in cavity ring-down spectroscopy: application to an optical detector for atmospheric no 2. *Applied Physics B: Lasers and Optics*, 81(1):135–141, 2005.

J. McManus, M. Zahniser, D. Nelson, L. Williams, and C. Kolb. Infrared laser spectrometer with balanced absorption for measurement of isotopic ratios of carbon gases. *Spectrochimica Acta Part A: Molecular and Biomolecular Spectroscopy*, 58(11):2465–2479, 2002.

J. Morville, S. Kassi, M. Chenevier, and D. Romanini. Fast, low-noise, mode-by-mode, cavity-enhanced absorption spectroscopy by diode-laser self-locking. *Applied Physics B: Lasers and Optics*, 80(8):1027–1038, 2005.

V. Motto-Ros, J. Morville, and P. Rairoux. Mode-by-mode optical feedback: cavity ringdown spectroscopy. *Applied Physics B: Lasers and Optics*, 87(3):531–538, 2007.

J. Paul, L. Lapson, and J. Anderson. Ultrasensitive absorption spectroscopy with a high-finesse optical cavity and off-axis alignment. *Applied Optics*, 40(27):4904–4910, 2001.

K. Petrov, S. Waltman, E. Dlugokencky, M. Arbore, M. Fejer, F. Tittel, and L. Hollberg. Precise measurement of methane in air using diode-pumped 3.4 μm difference-frequency generation in ppln. *Applied Physics B: Lasers and Optics*, 64(5):567–572, 1997.

P. Quay, J. Stutsman, D. Wilbur, A. Snover, et al. The isotopic composition of atmospheric methane. *Global Biogeochemical Cycles*, 13(2), 1999.

V. Ramanathan, R. Cicerone, H. Singh, and J. Kiehl. Trace gas trends and their potential role in climate change. *Journal of Geophysical Research-Atmospheres*, 90(D3), 1985.

R. Rasmussen and M. Khalil. Atmospheric methane in the recent and ancient atmospheres concentrations, trends, and interhemispheric gradient. *Journal of Geophysical Research*, 89:11599–11605, 1984.

W. Reeburgh. Global methane biogeochemistry. *Treatise on geochemistry*, 4:65–89, 2003.

A. Rice, A. Gotoh, H. Ajie, and S. Tyler. High-precision continuous-flow measurement of $\delta^{13}C$ and δD of atmospheric CH_4. *Anal. Chem*, 73(17):4104–4110, 2001.

A. Rice and P. Quay. Isotopic analysis of atmospheric formaldehyde by gas chromatography isotope ratio mass spectrometry. *Anal. Chem*, 78(18):6320–6326, 2006.

A. Rice, S. Tyler, M. McCarthy, K. Boering, and E. Atlas. Carbon and hydrogen isotopic compositions of stratospheric methane: 1. high-precision observations from the NASA ER-2 aircraft. *J. Geophys. Res*, 108:4460, 2003.

E. Richard, K. Kelly, R. Winkler, R. Wilson, T. Thompson, R. McLaughlin,
A. Schmeltekopf, and A. Tuck. A fast-response near-infrared tunable diode laser
absorption spectrometer for in situ measurements of CH_4 in the upper troposphere
and lower stratosphere. *Applied Physics B: Lasers and Optics*, 75(2):183–194, 2002.

J. Rogers and W. Whitman. Microbial production and consumption of greenhouse gases:
methane, nitrogen oxides, and halomethanes. In *Workshop on the microbial
production and consumption of radiatively important trace gases*, volume 14,
page 16, 1991.

D. Romanini, A. Kachanov, and F. Stoeckel. Diode laser cavity ring down spectroscopy.
Chemical Physics Letters, 270(5-6):538–545, 1997.

L. Rothman, D. Jacquemart, A. Barbe, D. Chris Benner, M. Birk, L. Brown, M. Carleer,
C. Chackerian, K. Chance, L. Coudert, et al. The HITRAN 2004 molecular
spectroscopic database. *Journal of Quantitative Spectroscopy and Radiative
Transfer*, 96(2):139–204, 2005.

L. Rothman, C. Rinsland, A. Goldman, S. Massie, D. Edwards, J. Flaud, A. Perrin,
C. Camy-Peyret, V. Dana, J. Mandin, et al. The HITRAN molecular spectroscopic
database: 1996 edition. *J. Quant. Spectrosc. Radiat. Transfer*, 60:665–710, 1996.

G. Saueressig, P. Bergamaschi, J. Crowley, H. Fischer, and G. Harris. Carbon kinetic
isotope effect in the reaction of CH_4 with Cl atoms. *Geophys. Res. Lett*, 22(10):1225,
1995.

G. Saueressig, P. Bergamaschi, J. Crowley, H. Fischer, and G. Harris. D/H kinetic
isotope effect in the reaction CH_4 + Cl. *Geophys. Res. Lett*, 23(24):3619, 1996.

G. Saueressig, J. Crowley, P. Bergamaschi, C. Brühl, C. Brenninkmeijer, and H. Fischer.
Carbon-13 and D kinetic isotope effects in the reactions of CH_4 with O(^{1}D) and OH:
New laboratory measurements and their implications for the isotopic composition of
stratospheric methane. *Journal of Geophysical Research-Atmospheres*, 106(D19),
2001.

M. Schupp, P. Bergamaschi, G. Harris, and P. Crutzen. Development of a tunable diode
laser absorption spectrometer for measurements of the $^{13}C/^{12}C$ ratio in methane.
Chemosphere, 26(1):13–22, 1993.

I. Simpson, D. Blake, F. Rowland, and T. Chen. Implications of the recent fluctuations in
the growth rate of tropospheric methane. *Atmosphere*, 315:0325.

A. Snover and P. Quay. Hydrogen and carbon kinetic isotope effects during soil uptake of
atmospheric methane. *Global Biogeochemical Cycles*, 14(1), 1999.

A. Snover, P. Quay, and W. Hao. The D/H content of methane emitted from biomass
burning. *Global Biogeochemical Cycles*, 14(1), 2000.

C. Stevens and M. Wahlen. The isotopic composition of athmospheric methane and its
sources. *Atmospheric Methane: Its role in the Global Environment. Springer-Verlag,
New York*, pages 25–41, 2000.

S. Tammela, H. Ludvigsen, T. Kajava, M. Kaivola, V. Electron, E. Mater, and F. Components. Time-resolved frequency chirp measurement using a silicon-wafer etalon. *IEEE Photonics Technology Letters*, 9(4):475–477, 1997.

M. Trudeau, P. Chen, G. de Andrade Garcia, L. Hollberg, and P. Tans. Stable isotopic analysis of atmospheric methane by infrared spectroscopy by use of diode laser difference-frequency generation. *Applied optics*, 45(17):4136–4141, 2006.

S. Tyler. The global methane budget. *Microbial production and consumption of greenhouse gases: methane, nitrogen oxides, and halomethanes*, page 7, 1991.

S. Tyler, H. Ajie, A. Rice, R. Cicerone, and E. Tuazon. Experimentally determined kinetic isotope effects in the reaction of ch4 with cl: Implications for atmospheric ch4. *Geophysical Research Letters*, 27(12), 2000.

S. Tyler, A. Rice, and H. Ajie. Stable isotope ratios in atmospheric CH_4: Implications for seasonal sources and sinks. *Journal of Geophysical Research-Atmospheres*, 112(D3):D03303, 2007.

K. Uehara, K. Yamamoto, T. Kikugawa, and N. Yoshida. Isotope analysis of environmental substances by a new laser-spectroscopic method utilizing different pathlengths. *Sensors & Actuators: B. Chemical*, 74(1-3):173–178, 2001.

S. Waltman, L. Hollberg, K. Petrov, F. Tittel, E. Dlugokencky, M. Arbore, and M. Fejer. Measurement of $^{13}CH_4/^{12}CH_4$ Ratios in Air Using Diode-Pumped 3. 3 µm Difference-Frequency Generation in PPLN. In *Proceedings of the 1997 IEEE/LEOS Summer Topical Meeting, Montreal (11–15 August 1997)*, 1997.

C. Webster and R. May. In situ stratospheric measurements of CH_4, $^{13}CH_4$, N_2O, and $OC^{18}O$ using the bliss tunable diode laser spectrometer. *Geophysical Research Letters*, 19(1):45–48, 1992.

M. Whiticar. Carbon and hydrogen isotope systematics of bacterial formation and oxidation of methane. *Chemical Geology*, 161(1-3):291–314, 1999.

M. Whiticar, "Chapter 5: Can stable isotopes and global budgets be used to constrain atmospheric methane budgets?" *Atmospheric methane: its role in the global environment*, page 63, 2000.

M. Whiticar, E. Faber, and M. Schoell. Biogenic methane formation in marine and freshwater environments: CO_2 reduction vs. acetate fermentation–isotope evidence. *Geochimica et Cosmochimica Acta*, 50:693–709, 1986.

M. Wolfsberg. Theoretical evaluation of experimentally observed isotope effects. *Accounts of Chemical Research*, 5(7):225–233, 1972.

D. Wuebbles, K. Hayhoe, and R. Kotamarthi. Methane in the global environment. *Atmospheric Methane: Sources, Sinks, and Role in Global Change, Springer-Verlag, New York*, pages 304–342, 2000.

K. Yamamoto and N. Yoshida. High-precision isotopic ratio measurement system for methane ($^{12}CH_3D/^{12}CH_4$,$^{13}CH_4/^{12}CH_4$) by using near-infrared diode laser absorption spectroscopy. *Spectrochimica Acta Part A: Molecular and Biomolecular Spectroscopy*, 58(12):2699 – 2707, 2002.

R. Zanasi, D. Alfano, C. Scarabino, O. Motta, R. Viglione, and A. Proto. Determination of $^{13}C/^{12}C$ carbon isotope ratio. *Anal. Chem*, 78(9):3080–3083, 2006.